

Two-photon coupling via Josephson element II: Interaction renormalizations and cross-Kerr coupling

E. V. Stolyarov ^{1,*} V. L. Andriichuk ² and A. M. Sokolov ^{2,†}

¹*Quantum Optics and Quantum Information Group, Bogolyubov Institute for Theoretical Physics, National Academy of Sciences of Ukraine, vul. Metrolohichna 14-b, Kyiv 03143, Ukraine*

²*Institute of Physics of the National Academy of Sciences, pr. Nauky 46, Kyiv 03028, Ukraine*

We study the interactions mediated by symmetric superconducting quantum interference device (SQUID), their renormalizations, and applicability of the anharmonic oscillator model for a coupled phase qubit. The coupling SQUID can switch between single- or two-photon interaction *in situ*. We consider a coupled resonator and an rf SQUID. The latter dwells in the vicinity of its metastable well holding a number of anharmonic energy states and acts as an artificial atom known as the phase qubit. Apart from the linear and two-photon couplings, interactions of optomechanical type and a cross-Kerr coupling arise. Near the two-photon resonance, we calculate the renormalizations due to nonresonant interactions, which are more prominent with the higher Josephson energy of the coupler. We interpret the renormalizations by depicting some of the virtual processes involved. That also allows us to determine the minimal amount of metastable states in the phase qubit for the renormalization formulas to hold.

I. INTRODUCTION

In a curious prediction of quantum theory, a real transition may occur in two steps with an intermediate state never occupied considerably; the two legs of such a process are called *virtual* transitions. In fact, one can even describe the simplest excitation exchange due to linear interaction as in Jaynes-Cummings model [1] in terms of two virtual processes: one destroying a quantum in the first system, and the other creating it in another system. In the respective approximation, the combined system is never found in the intermediate state. In a less trivial example, two nonresonant exchange interactions with an auxiliary system mediate a real excitation exchange between two other systems [2]; a modification [3, 4] of such a coupler powers a commercial quantum computer [5].

Virtual transitions can chain into more complex processes as well. Combined with intrinsic nonlinearity and transitions to the higher excited levels, linear interactions between transmon qubits [6] give rise to ZZ interaction [7]. Essentially, ZZ coupling is due to *parametric processes* [8] in which the system state does not change, but the system energy acquires dependency on the state of its parts. In the context of cavity [9, 10] and circuit quantum electrodynamics [11–13], an analogous coupling is known as dispersive. It arises due to virtual transition of a resonator photon into a qubit and back [12]. Two-photon interaction [14–20] facilitates single-mode squeezing [21]. It may be used for novel quantum information processing protocols [19] and achieving photon-number resolution in microwave photodetection [22–24]; With a deep strong two-photon coupling, interaction-induced spectral collapse may be observed [25]. Two-photon coupling can emerge—perturbatively—due to intermediate

virtual processes as predicted [16, 17, 22, 23, 26] and measured [26] for different systems.

To achieve high two-photon coupling rates one can either “simulate” it using the special driving schemes [21], or seek a nonlinear interaction strong enough so that it cannot be seen as a perturbation. In the preceding contribution [20], we argued that a symmetrical dc SQUID can mediate nonperturbative two-photon coupling of reasonable strength that arises directly from the Josephson nonlinearity. Independently, Ayyash *et al.* conveyed the same point in Ref. [19] for an asymmetrical SQUID. The latter is better suited for coupling circuits with zero static displacement of the superconducting condensate phase over them, such as resonator and transmon [6] qubit. However, in both works [19, 20], only the bare two-photon coupling was calculated; i.e. two-photon transitions due to possible virtual processes were not accounted for.

Moreover, neither of the works considered the cross-Kerr coupling. It arises with a parametric process similarly to the ZZ or dispersive coupling mentioned above. Typically, the term is used for two systems each having many energy states. This interaction is detrimental for applications of optomechanical systems [27] and traveling-wave parametric amplifiers [28]. In the absorbing detectors of microwave photons [29–40], cross-Kerr coupling introduces a photon-number-dependent detuning that may complicate the absorption. On the other hand, this very type of coupling is required for the quantum-nondemolition detection [41–48], dispersive qubit readout [11], and other applications for quantum computing with superconducting circuits [49].

In this work, we continue to study a resonator and a phase qubit coupled via the SQUID coupler (see Fig. 1). We answer the question: Having a plethora of different interactions and nonlinearities in that system, do they produce virtual transitions that yield a considerable correction to the two-photon coupling? Moreover, given its importance, we also study the cross-Kerr coupling in the system.

* E-mail: eugene.stolyarov@bitp.kyiv.ua

† E-mail: andriy145@gmail.com

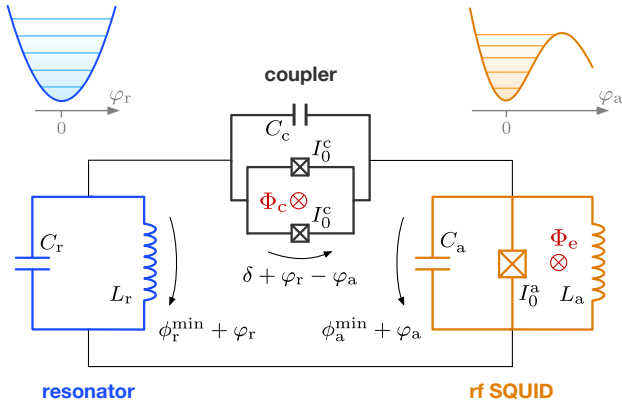


FIG. 1. A resonator and an rf SQUID in the regime of phase qubit interact through the SQUID coupler. The system evolves around the equilibrium phase differences ϕ_r^{\min} and ϕ_a^{\min} . The respective varying departures are φ_r and φ_a . Conjugated to them, dynamic variables n_r and n_a are the Cooper pair number at the full capacitances. $\delta = \phi_r^{\min} - \phi_a^{\min}$ is the equilibrium phase difference over the coupler. Φ_c and Φ_e are the coupler and rf SQUID bias fluxes. Cartoons show potentials and energy levels of the resonator (left) and the phase qubit (right).

The paper is organized as follows. We start with the approximate Hamiltonian of the circuit in Sec. II that is valid near the point of equilibrium. Then, in Sec. III, we present the effective two-photon Hamiltonian and outline the approximations we use. In Sec. IV, we elucidate how the two-photon and cross-Kerr interactions are renormalized by other couplings. We provide some related virtual processes in the form of diagrams. In Sec. V, we estimate the coupling rates for a reasonable set of circuit parameters. We additionally discuss our results in Sec. VI, provide some possible directions for future work in Sec. VII, and conclude in Sec. VIII. Derivation of the effective two-photon Hamiltonian that accounts for all relevant renor-

malizations is given in Appendix A. In Appendix B, we provide an alternative calculation of the main cross-Kerr correction using the Wick's theorem. We also provide further detail on laying out the diagrams for the virtual processes involved.

II. APPROXIMATE QUANTUM HAMILTONIAN

Consider the circuit in Fig. 1. It is convenient to describe the circuit dynamics in terms of dimensionless variables. Charge in the units of Cooper pairs acts as a generalized momentum, while the drop of the superconducting condensate phase acts as a generalized coordinate. By n_r , we denote the Cooper pair number on the resonator capacitance C_r . By n_a , we denote the similar rf SQUID variable. For it, the respective capacitance is the total one arising from the parallel connection of the junction and the shunting capacitances. Near the equilibrium, only the departures from the static values of the condensate phases do matter. φ_a is such a departure of the phase difference across the rf SQUID junction. φ_r is the phase departure across the resonator contacts.

A. First quantization

We derived the general circuit Hamiltonian in the preceding work [20], where the resulting expressions are given in Eqs. (1) and (4)–(6). Now we expand it around equilibrium, up to the fourth order in φ_r and φ_a . Then, we arrive at the quantized Hamiltonian

$$\hat{\mathcal{H}} = \hat{\mathcal{H}}_r + \hat{\mathcal{H}}_a + \hat{\mathcal{H}}_c, \quad (1)$$

by imposing the usual commutation relation $[\varphi_r, n_r] = i$ for the resonator variables and the analogous one for the rf SQUID. In the Hamiltonian in Eq. (1), the resonator, atom, and the coupling parts read

$$\hat{\mathcal{H}}_r \approx 4E_C^r n_r^2 + \frac{1}{2} \tilde{E}_L^r \varphi_r^2 - \frac{1}{6} E_J^c \varphi_r^3 \sin \delta - \frac{1}{24} E_J^c \varphi_r^4 \cos \delta, \quad (2)$$

$$\hat{\mathcal{H}}_a \approx 4E_C^a n_a^2 + \frac{1}{2} \tilde{E}_L^a \varphi_a^2 - \frac{1}{6} (E_J^a \sin \phi_a^{\min} - E_J^c \sin \delta) \varphi_a^3 - \frac{1}{24} (E_J^a \cos \phi_a^{\min} + E_J^c \cos \delta) \varphi_a^4, \quad (3)$$

$$\begin{aligned} \hat{\mathcal{H}}_c \approx & E_C^c n_a n_r - E_J^c \varphi_r \varphi_a \cos \delta, \\ & + \frac{1}{2} E_J^c (\varphi_r^2 \varphi_a - \varphi_r \varphi_a^2) \sin \delta - \frac{1}{4} E_J^c \varphi_r^2 \varphi_a^2 \cos \delta + \frac{1}{6} E_J^c (\varphi_r^3 \varphi_a + \varphi_r \varphi_a^3) \cos \delta. \end{aligned} \quad (4)$$

Each part consists of the “kinetic” energy contribution quadratic in n_r and n_a , the potential energy terms quadratic in φ_r and φ_a , and the higher-order terms that spawn self-nonlinearities and nonlinear interactions.

“Kinetic” energy terms are due to charging of the circuit capacitances. We denote $E_C^r = e^2/2\tilde{C}_r$ the resonator charging energy, where $\tilde{C}_r = C_r + C_a' C_c' / (C_a' + C_c')$. The latter expression describes the resonator capacitance

C_r loaded by the parallel connection with the atom full capacitance C'_a which is in series connection with the full coupling capacitance C'_c . It consists of the shunting and the junction capacitances, $C'_c = C_c + 2C_{1J}^c$. Analogously, for the artificial atom $E_C^a = e^2/2\tilde{C}_a$, where $\tilde{C}_a = C'_a + C_r C'_c / (C_r + C'_c)$ and $C'_a = C_a + 2C_{1J}$ with C_{1J} the internal capacitance of each of the coupler junctions. This exact expression for \tilde{C}_a is required in this work to tune the atom and resonator into the two-photon resonance. The coupler charging energy reads

$$E_C^c = 4e^2 \frac{\tilde{C}_c}{C'_a C_r}, \quad (5)$$

where the coupler capacitance is loaded by the parallel connection with the resonator and atom capacitances, $\tilde{C}_c = (1/C'_c + 1/C_r + 1/C'_a)^{-1} \approx C'_c$. The latter approximate equality qualifies as we have $C'_c \ll C_r, C'_a$ in Sec. V, similarly to the preceding work [20].

Nonlinear energy terms in Eqs. (2)–(4) are solely of the Josephson origin. We denote the atom Josephson energy by E_J^a . The coupler Josephson energy

$$E_J^c = 2E_{1J}^c \cos \frac{\pi \Phi_c}{\Phi_0} \quad (6)$$

can be tuned by the coupler bias Φ_c . On the other hand, it is set by the Josephson energy of each of the coupler junctions, $E_{1J}^c = I_0 \Phi_0 / 2\pi$, where I_0^c is the critical energy of the junction.

Finally, the contributions as from the linear inductances in Eqs. (2) and (3) express via the renormalized inductive-like energies

$$\tilde{E}_L^r = E_L^r + E_J^c \cos \delta, \quad (7a)$$

$$\tilde{E}_L^a = E_L^a + E_J^a \cos \phi_a^{\min} + E_J^c \cos \delta. \quad (7b)$$

Here $E_L^r = \Phi_0^2 / 4\pi^2 L_r$ is the resonator inductive energy and a similar expression holds for the atom inductive energy. According to Eq. (7a), the atom inductance L_r is loaded by the coupler Josephson inductance $L_c = \Phi_0^2 / (4\pi^2 E_J^c \cos \delta)$ as $\tilde{L}_r^{-1} = L_r^{-1} + L_c^{-1}$. Equation (7b) can be interpreted analogously.

This load depends on the equilibrium point. One quantity that defines this point is the static phase difference at the coupler,

$$\delta = \phi_r^{\min} - \phi_a^{\min} - \frac{\pi \Phi_c}{\Phi_0} \quad (8)$$

which depends on the coupler flux bias Φ_c . The equilibrium also directly depends on the static phase drops ϕ_a^{\min} and ϕ_r^{\min} at the atom and resonator. The latter are determined by the equations that describe the equilibrium,

$$E_L^r \phi_r^{\min} + E_J^c \sin \delta = 0, \quad (9a)$$

$$E_L^a \left(\phi_a^{\min} - \frac{2\pi \Phi_e}{\Phi_0} \right) + E_J^a \sin \phi_a^{\min} - E_J^c \sin \delta = 0, \quad (9b)$$

where Φ_e is the rf SQUID bias flux. As discussed in the preceding part [20], the equations express the conservation of currents. Alternatively, Eq. (9a) can be obtained by finding the screening current induced by the external magnetic field.

For the expansion of the energy terms as in Eqs. (2)–(4) to be valid, we require that the inductive-type energies dominate over the charging energies:

$$E_L^r \gg E_C^r, \quad E_J^a \gg E_C^a. \quad (10)$$

That assures the phase particles of both systems to be “heavy” and to reside close to the point of equilibrium.

Compared to the preceding work [20], we rearrange the terms in the Hamiltonians in Eqs. (2)–(4). Here the resonator and the atom Hamiltonians accommodate the nonlinearities due to the coupling SQUID. Moreover, here we do not neglect these nonlinearities right away, as they turn out to influence the resonance condition.

B. Second quantization

We express the system variables in terms of the bosonic ladder operators: $n_r = -in_{r,zpf}(a^\dagger - a)$ and $\varphi_r = \varphi_{r,zpf}(a^\dagger + a)$ for the resonator variables; while $n_a = -in_{a,zpf}(b^\dagger - b)$ and $\varphi_a = \varphi_{a,zpf}(b^\dagger + b)$ for the atom variables. Here, magnitudes of the resonator vacuum fluctuations read

$$n_{r,zpf} = (\tilde{E}_L^r / 32E_C^r)^{1/4}, \quad \varphi_{r,zpf} = (2E_C^r / \tilde{E}_L^r)^{1/4} \quad (11)$$

and the magnitudes of the atom vacuum fluctuations are

$$n_{a,zpf} = (\tilde{E}_L^a / 32E_C^a)^{1/4}, \quad \varphi_{a,zpf} = (2E_C^a / \tilde{E}_L^a)^{1/4}. \quad (12)$$

Hamiltonians of the resonator and artificial atom read

$$\hat{H}_r = \omega_r^p \left(a^\dagger a + \frac{1}{2} \right) - X_r (a^\dagger + a)^3 - Y_r (a^\dagger + a)^4, \quad (13)$$

$$\hat{H}_a = \omega_a^p \left(b^\dagger b + \frac{1}{2} \right) - X_a (b^\dagger + b)^3 - Y_a (b^\dagger + b)^4. \quad (14)$$

Here, the resonator and atom plasma frequencies are

$$\omega_r^p = \frac{1}{\hbar} \sqrt{8E_C^r \tilde{E}_L^r}, \quad \omega_a^p = \frac{1}{\hbar} \sqrt{8E_C^a \tilde{E}_L^a}, \quad (15)$$

where the renormalized inductive energies \tilde{E}_L^r and \tilde{E}_L^a are defined in Eqs. (7). We denote the full cubic and quartic self-nonlinearities in the atom Hamiltonian as X_a and Y_a . They include both the intrinsic nonlinearity and the nonlinearity induced by the coupling SQUID:

$$X_a = \frac{1}{6} \frac{E_J^a \sin \phi_a^{\min} - E_J^c \sin \delta}{\hbar} \varphi_{a,zpf}^3, \quad (16)$$

$$Y_a = \frac{1}{24} \frac{E_J^a \cos \phi_a^{\min} + E_J^c \cos \delta}{\hbar} \varphi_{a,zpf}^4.$$

The resonator self-nonlinearities

$$X_r = \frac{1}{6} \frac{E_J^c}{\hbar} \varphi_{r,zpf}^3 \sin \delta, \quad Y_r = \frac{1}{24} \frac{E_J^c}{\hbar} \varphi_{r,zpf}^4 \cos \delta \quad (17)$$

arise solely due to the coupling.

Now we rewrite the coupling Hamiltonian in Eq. (1) in terms of the ladder operators,

$$\begin{aligned} \frac{\hat{\mathcal{H}}_c}{\hbar} = & -g_1^c(a^\dagger - a)(b^\dagger - b) - g_1^i(a^\dagger + a)(b^\dagger + b) \\ & - \frac{K_0}{4}(a^\dagger + a)^2(b^\dagger + b)^2 \\ & - \sum_{n=2,3} g_n(a^\dagger + a)^n(b^\dagger + b) \\ & - \sum_{n=2,3} G_n(a^\dagger + a)(b^\dagger + b)^n. \end{aligned} \quad (18)$$

Here the first term describes the capacitive interaction of strength

$$g_1^c = \frac{E_C^c}{\hbar} n_{r,zpf} n_{a,zpf} \quad (19)$$

and the second term describes the bare inductive interaction with

$$g_1^i = \frac{E_J^c}{\hbar} \varphi_{r,zpf} \varphi_{a,zpf} \cos \delta. \quad (20)$$

These interactions are *dipolar*, while the remaining terms in Eq. (18) describe *non-dipolar* interactions arising due to nonlinear inductance of the SQUID coupler.

Of them, second line of Eq. (18) corresponds to the *bare* cross-Kerr interaction of strength

$$K_0 = \frac{E_J^c}{\hbar} \varphi_{r,zpf}^2 \varphi_{a,zpf}^2 \cos \delta, \quad (21)$$

as well as some other interactions that are nonresonant in our case. The third line describes, in particular, conversion of n resonator photons into the atom excitation and vice versa. Coupling strengths for $n = 2$ and $n = 3$ are

$$g_2 = -\frac{1}{2} \frac{E_J^c}{\hbar} \varphi_{r,zpf}^2 \varphi_{a,zpf} \sin \delta, \quad (22)$$

$$g_3 = -\frac{1}{6} \frac{E_J^c}{\hbar} \varphi_{r,zpf}^3 \varphi_{a,zpf} \cos \delta. \quad (23)$$

The last term in Eq. (18) describes, in particular, creation of n excitations in the artificial atom by a single resonator photon and vice versa. We introduce

$$G_2 = \frac{1}{2} \frac{E_J^c}{\hbar} \varphi_{r,zpf} \varphi_{a,zpf}^2 \sin \delta, \quad (24)$$

$$G_3 = -\frac{1}{6} \frac{E_J^c}{\hbar} \varphi_{r,zpf} \varphi_{a,zpf}^3 \cos \delta \quad (25)$$

to denote the rates of these interactions.

Note the signs of some terms in the Hamiltonians in Eqs. (13), (14), and (18). We choose them so that the important interaction rates $g_2, K_0 > 0$ when the two-photon coupling strength g_2 attains its highest value (see Fig. 6). That is especially convenient in what follows, for reading whether the renormalization terms increase or decrease their *magnitude*. By the same reason, $X_a, X_r > 0$, as these quantities frequently appear in the rate renormalizations.

III. EFFECTIVE HAMILTONIAN

In this section, we do not detail the coupler regime. That is, we provide the expressions for the coupling rates for an arbitrary coupler phase δ as given by Eq. (8). We only require that one adjusts the artificial atom and the resonator to the two-photon resonance $\tilde{\omega}_a \approx 2\tilde{\omega}_r$. Here and below in the main text, $\tilde{\omega}_a$ and $\tilde{\omega}_r$ stand for actual frequencies of the atom and resonator.

Close to the two-photon resonance, their dynamics is governed by the Hamiltonian

$$\begin{aligned} \frac{\hat{\mathcal{H}}}{\hbar} = & \tilde{\omega}_r a^\dagger a + \tilde{\omega}_a b^\dagger b - \frac{\Xi_a}{2} b^{\dagger 2} b^2 \\ & - \tilde{K} a^\dagger a b^\dagger b - \tilde{g}_2 (a^{\dagger 2} b + b^\dagger a^2). \end{aligned} \quad (26)$$

It is a generalization of a two-photon Jaynes-Cummings model with a two-photon coupling rate \tilde{g}_2 and an additional cross-Kerr interaction of strength \tilde{K} . Due to the two-photon coupling, annihilation of two resonator photons excites the artificial atom, and vice versa. In contrast to the standard two-photon Jaynes-Cummings model [50, 51], we describe the artificial atom as an oscillator of anharmonicity Ξ_a rather than a two-level system. We derive Hamiltonian (26) in Appendix A while calculating the renormalizations in its parameters perturbatively.

Next, we outline the approximations we have used. Afterwards, we provide expressions for the interaction rates in Hamiltonian (26) in Sec. IV and approximate expressions for the frequencies in Sec. V C.

A. Approximations and the limits of validity

Besides the intrinsic nonlinearities in Eqs. (16) and (17), there are nonlinearities induced by the Josephson coupler. We assume that the induced *cubic* nonlinearities are much weaker than the cubic nonlinearity of the artificial atom. We neglect them in the coupling rates assuming that the condition $E_J^c \ll \tilde{E}_L^a$ yields a reasonable accuracy in determining the rates.

As explained before, we expand the coupling terms in the Hamiltonian in the fourth order in the system phases. In other words, we assume that the phase zero-point fluctuations are small, each system holds only a relatively small number of excitations, and the SQUID nonlinearity is reasonably bounded from above.

Particularly, we require that the inductive coupling is not in the ultrastrong regime, i.e. $g_1^i \ll \omega_a^p$. We rewrite that condition to obtain

$$\frac{E_J^c}{\tilde{E}_L^a} \ll \frac{2\varphi_{a,zpf}}{\varphi_{r,zpf}} \quad (27)$$

using Eqs. (20), (15), and (12).

As already mentioned, we focus on the case of two-photon resonance, $\tilde{\omega}_a \approx 2\tilde{\omega}_r$. Resonance occurs when the

detuning between the two interacting systems is either smaller than their linewidths or the interaction rate. On the other hand, we assume that the atom single-photon transition is highly nonresonant and we treat the linear interaction as a perturbation. Same considers the optomechanical-type interactions: the system should not be driven in a way that produces transitions such as typically used for the radiative cooling and amplification [52, 53].

Finally, for calculations in Appendix A, the artificial atom holds an infinite amount of the energy levels with the same anharmonicity. An analogous approximation is routinely used for the transmon artificial atom [13], which normally possesses about ten energy levels [54]. Recently, this approximation limits were studied for a transmon in dispersive readout [54]. In this paper, we make estimates for an rf SQUID with merely seven metastable states in Sec. V. We further discuss the bosonic approximation in Sec. VI.

IV. RELEVANT INTERACTIONS

Here we provide our analytical results for the resonant two-photon and cross-Kerr interactions as given in the Hamiltonian in Eq. (26), as well as for other relevant nonresonant interactions. Alongside to the expressions, we provide the diagrams to illustrate some virtual transitions that modify the bare interaction rates. These diagrams are related to the Feynman diagrams, which were already studied in the context of Schrieffer-Wolff transformations [55, 56]. Note that we do not show the real particles of an interaction with free legs as in Feynman diagrams. Instead, we show the energy states the system virtually goes through during the full interaction process. That allows us to clearly illustrate the smallest possible number of energy states for a given process to occur at all.

A. Non-resonant dipolar interactions

While we assume that the linear interactions are strongly nonresonant, they do provide significant renormalizations in our model. Besides, they can become relevant if the coupler is used with a multimode resonator or a waveguide. There is a dipolar coupling of capacitive origin with a strength g_1^c as given by Eq. (19). According to Eqs. (19) and (5), it arises due to the junction self-capacitances C_j^c in the coupler and a possible shunting capacitance C_c there. As we explain below, this coupling does not renormalize due to other interactions or the atom nonlinearity.

On contrary, inductive interaction mediated by the SQUID coupler does renormalize. According to Ap-

pendix A 2, it acquires the rate of

$$\tilde{g}_1^i \approx g_1^i - \frac{20G_2X_a}{\omega_a^p} \quad (28)$$

$$= \frac{E_J^c}{\hbar} \left(\cos \delta - \frac{5}{6} \mu \varphi_{a,zpf}^2 \sin \delta \right) \varphi_{r,zpf} \varphi_{a,zpf}. \quad (29)$$

We provide the dominant terms for both parts proportional to $\cos \delta$ and $\sin \delta$. The first term in Eq. (28) is the rate of bare inductive interaction due to the coupler Josephson inductance, as given by Eq. (20). When $\delta \bmod \pi = \pi/2$, this bare coupling vanishes. Hence the second term in Eq. (28) becomes dominant close to that point.

As follows from the calculation in Appendix A 1, the second term in Eq. (28) arises with the dressing of the atom in the harmonic approximation by the interactions with itself. Namely, this occurs via its cubic nonlinearity as given in Eq. (14). That dressing spawns the correction to the linear coupling out of the interaction G_2 in Eq. (18).

In Eq. (7), the cubic nonlinearity in the atom potential is characterized by the coefficient

$$\mu = \frac{12X_a}{\varphi_{a,zpf} \omega_a^p} \approx \frac{E_J^a}{\tilde{E}_L^a} \sin \phi_a^{\min}, \quad (30)$$

where we have taken into account that $2\tilde{E}_L^a/\hbar\omega_a^p = \varphi_{a,zpf}^{-2}$. When $\mu \sim 1$, order of the \tilde{g}_1^i correction in the zero-point fluctuations is as explicitly captured by Eq. (29).

In Eq. (30), we have neglected a term that is proportional to the coupler Josephson energy E_J^c . It arises with the nonlinearity induced by the coupler as in Eqs. (16). We neglect the induced nonlinearity of the resonator as in Eq. (9a) in the coupling rates. Hence, this induced nonlinearity in the atom is also to be neglected in Eq. (30) which is used solely for calculation of the coupling rates.

The correction to the inductive single-photon coupling in Eqs. (28) and (29) can be further understood as follows. It arises as the virtual transitions due to the G_2 interaction chain with the transitions due to the atom nonlinearity. Out of many such processes, we illustrate in Fig. 2(I) the one that excites the atom as high as possible. (More precisely, when reading from right to left and from left to right, each diagram in Figs. 2 and 3 shows *two* Hermitian-conjugated processes.)

It is important for the correction in Eq. (29) that four atom processes contract into two vacuum loops. That allows for the required \sqrt{m} coefficient when the full sequence acts on an atom excited state $\propto b^{\dagger m}|g\rangle$. Moreover, in Fig. 2(I), we put the loops one above each other. That corresponds to the vacuum part of the $b^2b^{\dagger 2}$ process when reading the diagram from right to left. We parallel the contractions shown with the loops to the contractions in the Wick's theorem in Appendix B.

Note that there are no corrections to the capacitive single-photon coupling in our model. The reason is that both the atom nonlinearity in Eq. (14) and the optomechanical energy in Eq. (18) are of inductive type alone,

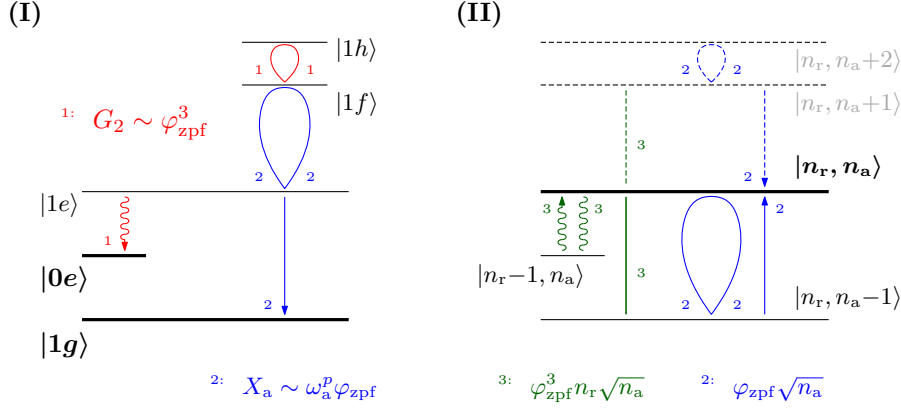


FIG. 2. Some corrections to the bare linear and cross-Kerr couplings. (I) Inductive single-photon corrections arise due to combination of the optomechanical interaction G_2 with the energy quadratic in the atom variables (1, red) and the atom cubic nonlinearity X_a (2, blue). (II) Cross-Kerr corrections arise due to optomechanical coupling g_2 with the energy quadratic in the resonator variables (3, green) and the atom cubic nonlinearity. Each part of the process contributes to its full amplitude $\sim n_r n_a$. First index in a state label corresponds to the number of the resonator energy level, whereas the second one labels the atom level. Dashed lines correspond to an alternative process path that reaches highest energies. The wavy lines stand for creation or annihilation of a resonator photon, while the straight lines denote the atom processes. Each diagram can be read from left to right and vice versa, as indicated by the arrows at the start and end of the respective processes. Loops contract creation and annihilation, such that only vacuum parts contribute—i.e. the unity in $bb^\dagger = 1 + b^\dagger b$. For brevity, vacuum fluctuations are equal in the atom and resonator, $\varphi_{a,\text{zpf}} = \varphi_{r,\text{zpf}} = \varphi_{\text{zpf}}$ and $n_{a,\text{zpf}} = n_{r,\text{zpf}} = n_{\text{zpf}}$. Each virtual process brings a relevant factor (in corresponding colors and positions) to the full amplitude.

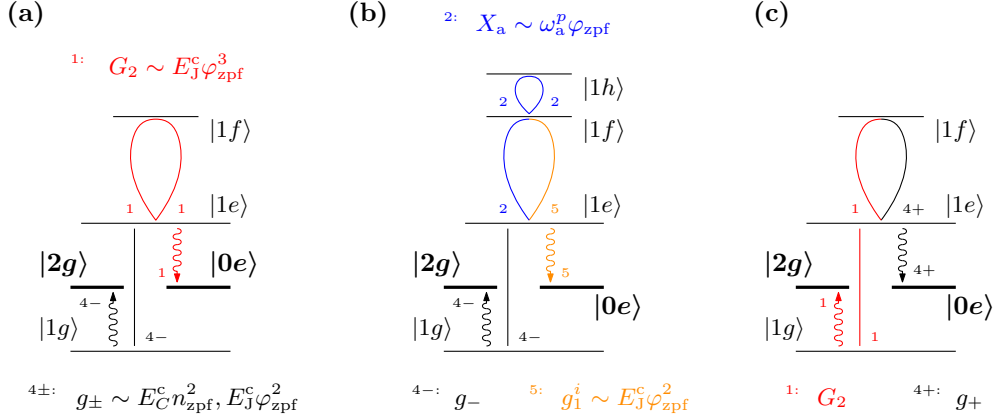


FIG. 3. Some corrections to the two-photon coupling. (a) Virtual transitions $0e \leftrightarrow 1e$ and $1e \leftrightarrow 2g$ mediated by the number-conserving linear coupling g_- (4- black) and the optomechanical coupling G_2 (1, red). (b) Virtual transitions $2g \leftrightarrow 1e$ with the number-conserving linear coupling and $1e \leftrightarrow 0e$ with the atom cubic nonlinearity X_a (2, blue) and the number-nonconserving part of the linear inductive coupling g_1^i (5, orange). (c) Virtual transitions $0e \leftrightarrow 1e$ and $1e \leftrightarrow 2g$ mediated by the two-atom-excitation coupling G_2 and the number-nonconserving linear inductive interaction g_+ (4+ black). Other notations as in Fig. 2.

i.e. they depend only on the atom phase variable $\propto b^\dagger + b$. When combining, they only result in inductive interactions.

B. Number-conserving and nonconserving linear interactions

It is also convenient to view the linear couplings from a different perspective. Inductive coupling with the energy $-\hbar\tilde{g}_1^i(a+a^\dagger)(b+b^\dagger)$ combines with the capacitive coupling of energy $-\hbar g_1^c(a-a^\dagger)(b-b^\dagger)$ defined in Eq. (18). As a result, an excitation may transit from one system to another with the rate of

$$g_- = g_1^c - \tilde{g}_1^i. \quad (31)$$

Alternatively, with the rate of

$$g_+ = g_1^c + \tilde{g}_1^i \quad (32)$$

both the resonator and the atom may simultaneously excite or de-excite by one energy level. The first nonresonant process conserves the excitation number, while the second does not.

C. Non-resonant optomechanical interactions

Interaction term with G_2 in Eq. (18) describes, in particular, an optomechanical type of interaction where the atom plays the role of an optical cavity. Its frequency is modulated by the generalized coordinate of the microwave resonator that plays a role of a mechanical mode. Owing to a combination of inductive interactions with the atom cubic nonlinearity, this coupling strength renormalizes as $G_2 \rightarrow J$ with the full coupling rate

$$J = G_2 + \frac{6g_1^i X_a}{\omega_a^p} \quad (33)$$

$$\approx \frac{1}{2} \frac{E_J^c}{\hbar} (\sin \delta - \mu \cos \delta) \varphi_{r,zpf} \varphi_{a,zpf}^2, \quad (34)$$

whereas its bare rate G_2 is given in Eqs. (24). This correction to the G_2 interaction can be interpreted similarly as in Eq. (28).

Consider also the coupling of strength g_2 as in Eq. (18) that is symmetrical to G_2 . It also yields an optomechanical interaction, albeit with the reversed roles of the microwave resonator and atom. However, within our assumptions, this optomechanical interaction does not renormalize and retains its bare magnitude as in Eq. (22). This asymmetry, as seen in Eqs. (22) and (33), is due to the cubic nonlinearity in the potential of the artificial atom that the resonator, in fact, lacks. In Eq. (34), the atom nonlinearity is characterized by μ as given by Eq. (30).

Next we turn to the resonant interactions. They are described by the last two terms in the effective Hamiltonian (26).

D. Cross-Kerr coupling

First, consider how the cross-Kerr coupling renormalizes directly due to the cubic perturbation in the atom potential,

$$K_{0,X} = K_0 + \frac{24g_2 X_a}{\omega_a^p} \quad (35)$$

$$= \frac{E_J^c}{\hbar} (\cos \delta - \mu \sin \delta) \varphi_{r,zpf}^2 \varphi_{a,zpf}^2. \quad (36)$$

The renormalization occurs similarly to that for the linear interaction in Eq. (28). Following the Schrieffer-Wolff transformation in Appendix A 1, the atom self-dressing due to its potential cubic nonlinearity spawns the cross-Kerr correction out of the optomechanical interaction of rate g_2 .

In a more physical picture, the correction occurs owing to the virtual processes. The virtual optomechanical transitions of rate g_2 chain with the transitions caused by the atom nonlinearity. We illustrate some example processes in Fig. 2(II). Just as for the correction in the linear inductive coupling rate, it is important here that two atom processes contract into a vacuum loop. We provide some formal background for laying out the cross-Kerr correcting diagrams in Appendix B.

In the optomechanical processes of the correction in Eq. (35), resonator acts as an optical cavity and the artificial atom acts as a mechanical mode. Notice that there are no optomechanical processes of rate G_2 in which the roles are reversed. That is the case as we neglect cubic anharmonicity in the resonator potential. The asymmetry in Eq. (28) arises with the same reason.

The full cross-Kerr coupling also includes corrections solely from the interactions. For them, we do not point out the virtual processes involved, as they are small for the estimates in Sec. V. The full cross-Kerr coupling strength in the effective Hamiltonian Eq. (26) is

$$\tilde{K} = K_{0,X} + K_{\text{lin}} + K_{\text{mix}} + K_{\text{quad}}. \quad (37)$$

Here, K_{lin} is the part induced by the linear interactions. K_{mix} arises as the linear interactions interplay with the nonlinear ones having the energy cubic in the atom variables. K_{quad} comes from the nonlinear couplings with the energy quadratic in either of the system variables.

First consider the corrections induced by the linear interaction,

$$K_{\text{lin}} = \frac{2\Xi_a g_-^2}{(\tilde{\omega}_a - \tilde{\omega}_r)(\tilde{\omega}_a - \tilde{\omega}_r - \Xi_a)} + \frac{2\Xi_a g_+^2}{(\tilde{\omega}_a + \tilde{\omega}_r)(\tilde{\omega}_a + \tilde{\omega}_r - \Xi_a)}. \quad (38)$$

The first term here is the same as for the Stark shift in the dispersively coupled transmon and resonator [6, 13]. The second term arises due to the number-nonconserving terms in the linear coupling. It is comparable to the contribution of the co-rotating terms due to a large detuning

$\tilde{\omega}_a - \tilde{\omega}_r \approx \tilde{\omega}_r$. A shift of the same nature also enters the rate of linear interaction mediated by a transmon coupler [2, 3].

For a high atom anharmonicity $|\Xi_a| \gg |\tilde{\omega}_a - \tilde{\omega}_r|$, the first term in Eq. (38) describes the dispersive coupling with a *two-level* qubit and a resonator [11, 12]. If, furthermore, higher atom energies are sparser with $\Xi_a < 0$, while $-\Xi_a \gg \tilde{\omega}_r$, the second term in Eq. (38) recovers the correction [57–59] beyond the rotating-wave approximation for the two-level qubit. When comparing with the literature, mind the “–” sign in our definition of the cross-Kerr coupling rate in the Hamiltonian Eq. (18).

Existence of the other terms in Eq. (37) rely on various nonlinear interactions. We provide them in the assumption of relatively small atom anharmonicity, $|\Xi_a| \ll \omega_r, \omega_a$. While our treatment in Appendix A 2 may be extended to obtain the more general form of these terms, that is of little value for this work.

Consider the term due to the interplay of the linear and nonlinear interactions,

$$K_{\text{mix}} = 4 \left(\frac{g_-}{\tilde{\omega}_a - \tilde{\omega}_r} + \frac{g_+}{\tilde{\omega}_a + \tilde{\omega}_r} \right) F, \quad (39)$$

where

$$F = 3G_3 + \frac{5}{3} \mu \varphi_{a,\text{zpf}} G_2 \quad (40)$$

is the rate of the nonlinear interaction that causes the same transitions as the linear coupling. Namely, this interaction is described by three atom operators and a single photon one as explained in Appendix A 2. Its bare rate $3G_3$ renormalizes similarly to the inductive coupling in Sec. IV A.

According to the Schrieffer-Wolff transformation in Appendix A 2 a, the cross-Kerr correction in Eq. (39) arises with the mutual dressing of the atom and resonator. Here it occurs due to the linear coupling and its nonlinear counterpart of the rate F . On such a dressing, these interactions spawn the cross-Kerr correction.

Finally, we provide the corrections solely from the nonlinear interactions,

$$K_{\text{quad}} = \frac{4g_2^2}{\tilde{\omega}_a + 2\tilde{\omega}_r} + \frac{16g_2^2\Xi_a}{\tilde{\omega}_a^2} + \frac{4(\tilde{G}_2^-)^2}{2\tilde{\omega}_a - \tilde{\omega}_r} + \frac{4(\tilde{G}_2^+)^2}{2\tilde{\omega}_a + \tilde{\omega}_r}. \quad (41)$$

The first term here stems from the nonresonant part of the bare two-photon coupling g_2 from Eq. (18). The second term spawns from the atom anharmonicity as the atom dresses due to the optomechanical coupling of rate g_2 . The last two terms are induced by the interaction that exchanges two atom excitations for a single photon. It origins from the bare interaction term of rate G_2 in Eq. (18) and its renormalization as in (see Appendix A 2)

$$\tilde{G}_2^\pm = G_2 - \frac{1}{6} \mu \varphi_{a,\text{zpf}} (g_1^i \pm 2g_1^e). \quad (42)$$

The renormalization in \tilde{G}_2^\pm spawns from the capacitive and inductive couplings as the atom dresses by its cubic nonlinearity.

The corrections in K_{mix} and K_{quad} are of the sixth order in the zero-point fluctuations $\varphi_{r,\text{zpf}}$ and $\varphi_{a,\text{zpf}}$. Formally, that exceeds accuracy of the expansion [20] of the coupler Josephson energy as given by the Hamiltonian in Eq. (18). However, they can still be larger than the neglected terms in the expansion. That is the case when $\varphi_{\text{zpf}} E_J^c / \tilde{\omega}_r \gtrsim 1$, where φ_{zpf} is either of $\varphi_{r,\text{zpf}}$ or $\varphi_{a,\text{zpf}}$. Therefore, these sixth-order terms become significant if the Josephson coupling is strong enough.

E. Two-photon coupling

Finally, we provide the expression for the two-photon coupling rate in Eq. (26),

$$\tilde{g}_2 = g_2 - \frac{2g_- J}{\tilde{\omega}_r} + \frac{2g_+ G_2}{3\tilde{\omega}_r} - \frac{\mu \varphi_{a,\text{zpf}} g_+ (g_1^i - 2g_1^e)}{9\tilde{\omega}_r}. \quad (43)$$

This expression assumes relatively small atom anharmonicity, $|\Xi_a| \ll \omega_a$. The first term in Eq. (43) comes from the *bare* two-photon coupling g_2 . It originates solely from the expansion of the coupler Josephson energy, as given by Eq. (22). The other terms are due to various perturbative corrections as discussed below.

They are of the fifth order in the zero-point fluctuations $\varphi_{r,\text{zpf}}$ and $\varphi_{a,\text{zpf}}$ and hence formally below the accuracy of the expansion in Eq. (18). However, just like the corrections in Eqs. (39) and (41), they exceed the respective expansion terms if the Josephson coupling is strong enough. On the other hand, we neglect the sixth-order corrections (see Appendix A 2) as they are comparable to the fourth-order expansion terms for even higher coupling energies as in $\varphi_{\text{zpf}}^2 E_J^c / \tilde{\omega}_r \gtrsim 1$. By the similar reasons, one may use $g_\pm \approx g_1^e \pm g_1^i$ in Eq. (43). That is, the inductive coupling rate can be taken without renormalizations at its bare value of g_1^i as in Eq. (20).

Consider the correction in the second term in Eq. (43). In the language of the Schrieffer-Wolff transformations (see Appendix A), it arises as the single-photon and optomechanical interactions spawn the two-photon interaction after the atom and the resonator dress due to these very interactions. More physically, this correction is due to chaining of the single-photon and optomechanical virtual processes. We depict one such sequence with a bare optomechanical process in Fig. 3(a). Another one arises through its dressed part in Eq. (33). In other words, linear inductive interaction chains with the full number-conserving one and the atom cubic nonlinearity. We depict one such sequence with a number-nonconserving part of the inductive interaction in Fig. 3(b). Note how operators from different interactions can contribute to a vacuum loop.

The correction as in the third term in Eq. (43) can be depicted similarly to the second term, see Fig. 3(c). Here, however, a G_2 interaction that doubly (de-)excites the atom chains with the number-nonconserving linear interaction. As before, in Fig. 3(c) we choose the partic-

ular processes so that the other similar ones do not excite the atom higher.

Now consider the two-photon correction in the last term in Eq. (43). It arises, among others, owing to a process similar to that in Fig. 3(b) and uses five energy states of the atom. This term is considerably smaller than the other corrections, owing to the coefficient of $\mu/9$. Still, the term can be significant with even smaller zero-point fluctuations or when the capacitive coupling is much stronger than the inductive one $g_1^c \gg g_1^i$.

The latter case is unlikely when one aims at stronger two-photon coupling. We expect g_1^c to be of the same order or smaller than the maximal value of the inductive coupling rate $(g_1^i)_{\max}$. Both couplings are limited by the criterion $g_- = g_1^c - \tilde{g}_1^i \ll \tilde{\omega}_r, \tilde{\omega}_a$ disallowing ultrastrong coupling. Practically, one raises the coupler Josephson energy E_J^c to reach higher two-photon coupling strength $g_2 \propto E_J^c$; that raises $g_1^i \propto E_J^c$ proportionally. Hence, for such an application, it is unlikely that $g_1^c \gg (g_1^i)_{\max}$, as that severely limits the magnitude of $(g_1^i)_{\max}$ and g_2 .

Under reasonable circumstances, the full correction in Eq. (43) is small compared to the bare two-photon coupling g_2 . Indeed, $g_- \ll \tilde{\omega}_r$ as we require the coupling strength below the ultrastrong regime. On the other hand, one may expect $G_2, J \sim g_2$ according to Eqs. (33) and (24). That is the case when the resonator and the atom zero-point fluctuations are of the same order of magnitude, $\varphi_{r,zpf} \sim \varphi_{a,zpf}$. In the other case with $\varphi_{r,zpf} \ll \varphi_{a,zpf}$, the correction in Eq. (43) can be of the same order as the bare two-photon coupling.

V. NUMERICAL ESTIMATES

In this section, we apply our theory to a specific type of artificial atom, a flux-biased phase qubit [60], which can be used as a microwave photodetector—a Josephson photomultiplier [31, 32]. We explain how we choose reasonable circuit parameters matching the two-photon resonance. Then we examine how the coupler bias influences the relevant interaction rates. Also, we determine and analyze the magnitude of particular contributions to these rates.

A. Phase qubit regime of the rf SQUID

The exact expression for the isolated rf SQUID potential energy reads

$$U_a = \frac{E_L^a}{2} \left(\phi_a - \frac{2\pi\Phi_e}{\Phi_0} \right)^2 - E_J^a \cos \phi_a. \quad (44)$$

In the phase qubit regime, the rf SQUID features a strongly asymmetric two-well potential. Its shallow well contains only a few energy levels. Moreover, the rf SQUID is initially prepared to reside in its metastable well. The potential and energy levels are shown in Fig. 4

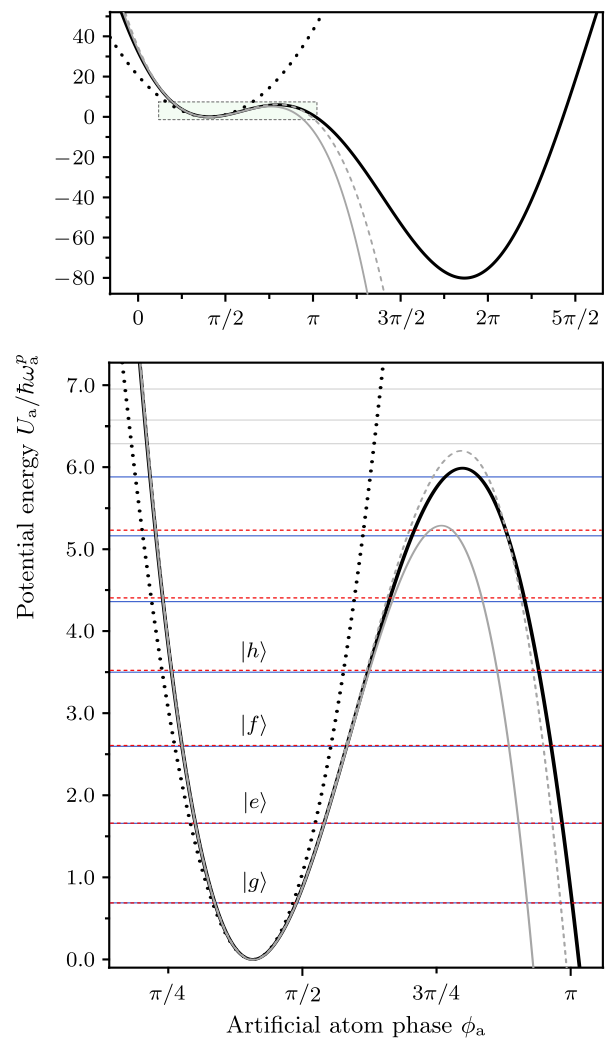


FIG. 4. (Top panel) Double-well potential (thick black) of the uncoupled rf SQUID as given by Eq. (44). Other curves show the potential in the harmonic (dotted), cubic (thin dashed), and quartic (thin solid) approximations. The energy origin is at the bottom of the left well. Shaded rectangle highlights the region shown in the other panel. (Bottom panel) Metastable well hosting levels $|g\rangle$, $|e\rangle$, $|f\rangle$, $|h\rangle$, and three others. Solid lines indicate the energies of metastable states and several over-the-barrier states, selected among numerical solutions of the stationary Schrödinger equation for the full potential. Dashed lines indicate the energy levels according to the perturbation theory as in Eq. (45). Parameters: $E_J^a/E_L^a = 3.950 \times 10^{-4}$, $E_J^c/E_L^c = 3.3424$, and $\Phi_e = 0.7150\Phi_0$.

for the uncoupled rf SQUID. Turning on the Josephson coupling only renormalizes the atom Josephson inductance. According to Eq. (7b), that distorts the potential only slightly when $E_J^c \ll E_L^a + E_J^a \cos \phi_a^{\min}$. For the energy ratios and external flux as in the Fig. 4 caption, the atom equilibrium phase is $\phi_a^{\min} \approx 0.4091\pi$. Hence the atom Josephson energy improves the criterion by about $E_J^c \cos \phi_a^{\min} \approx 0.9411E_L^a$.

In this subsection and in Sec. V C, we first provide the

energies and frequencies for the isolated systems. That is, $E_J^c = 0$ both for determining the inductive energies in Eqs. (7) and the equilibria in Eqs. (9), while $C_c' = 0$ for determining the capacitive energies.

We choose the rf SQUID inductance $L_a = 1.0000$ nH ($E_L^a/h = 163.46$ GHz) and critical current $I_0^a = 1.1000$ μ A ($E_J^a/h = 546.35$ GHz) close to Ref. [31]. However, we pick a smaller full capacitance of the artificial atom $C_a' = 300.0$ fF ($E_C^a/h = 64.57$ MHz) to increase its anharmonicity. The rf SQUID external flux is indicated in Fig. 4. These parameters yield the plasma frequency of the metastable well $\omega_a^p = 2\pi 12.80$ GHz and the magnitudes of zero-point fluctuations $n_{a,zpf} = 3.520$ and $\varphi_{a,zpf} = 0.1420$. Anharmonicity of the metastable energy levels is $[(E_e - E_g) - (E_f - E_e)]/h = 391.28$ MHz, as calculated directly from the eigenenergies of the three lowest levels $E_{g,e,f}$ according to numerical solution of the Schrödinger equation. On the other hand, perturbative estimate according to Eq. (46) yields $\Xi_a = 325.04$ MHz.

Note, that for the capacitance density of 50 fF/ μ m² in a Josephson junction and its critical current density of 1.7 μ A/ μ m² [15, 60], self-capacitance of the atom junction is about 32 fF for our choice of the critical current I_0^a . Thus, to achieve the total capacitance of the rf SQUID as above, one requires a shunting capacitance of about 170 fF.

Notice how the perturbative energy levels in Fig. 4 compare to the levels we calculate numerically. The perturbative results there are according to the second-quantized Hamiltonian (A4) in Appendix A. A discrepancy with the exact calculation is only visible close to the barrier top. That happens as the potential nonlinearities become comparable to the harmonic approximation. For the highest metastable level, the well becomes significantly wider than the harmonic approximation, while the barrier becomes so thin that the wavefunction spreads into it considerably deeper. Hence the state energy is lower compared to the perturbation theory result, as seen in the figure.

Moreover, the perturbative theory misses one metastable level altogether. We calculate the perturbative energy levels for the fourth-order approximation to the potential. It breaks vividly near the barrier top (see Fig. 4) and hence misses one metastable level. Note that the cubic approximation happens to work better near the barrier top. However, we use the fourth-order one, as we are more interested in predicting the lowest transition frequency analytically.

B. Coupler parameters

We choose a moderate value of the coupler Josephson energy. Each of its junctions with critical current $I_0^c = 30$ nA possesses the energy of $E_{1J}^c/h \approx 14.90$ GHz. With capacitance $C_c' = 5$ fF ($E_C^c/h \approx 2.70$ MHz), the coupler mediates a capacitive coupling with a rate of about $2\pi 50$ MHz well-attainable in circuit quantum elec-

trodynamic [61, 62].

We consider coupler Josephson energy that is relatively small compared to other respective energies that are relevant for determining the transition frequencies, $2E_{1J}^c \sim 0.1(E_L^a + E_J^a \cos \phi_a^{\min}), 0.1E_L^r$. Still, variation of this coupler energy may bring the system off-resonance. Indeed, $2E_{1J}^c$ shifts both the atom and the resonator full inductive energies as in Eqs. (7). Depending on the coupler bias Φ_c , that yields a variation in the detuning $\tilde{\omega}_a - 2\tilde{\omega}_r \sim \omega_a^p - 2\omega_r^p$ of up to about $E_{1J}^c |\omega_a^p/E_J^a - 2\omega_r^p/E_L^r| \sim 0.1\omega_a^p$. Under normal circumstances, this far exceeds both the linewidths and the two-photon coupling rate \tilde{g}_2 . That said, we aim for the resonance to occur close to the coupler bias with the highest two-photon coupling rate \tilde{g}_2 .

C. Resonator parameters and analytics for the resonance position

We choose the resonator parameters to hit the resonance as described below. In addition, we fix the resonator and atom zero-point phase fluctuations to have close amplitudes. We arrive at the resonator inductance $L_r = 0.84868$ nH ($E_L^r/h = 192.61$ GHz) and capacitance $C_r = 692.8$ fF ($E_C^r/h = 27.05$ MHz). For uncoupled resonator, this yields plasma frequency $\omega_r^p = 2\pi 6.56$ GHz and zero-point fluctuations with amplitudes $n_{r,zpf} = 3.830$ and $\varphi_{r,zpf} = 0.1305$.

When the inductive component of the coupling is fully turned on with $E_J^c = 2E_{1J}^c$, the two-photon coupling rate \tilde{g}_2 is close to its maximum (see also Fig. 6). Hence we choose the resonator parameters so that the analytical approximation predicts the two-photon resonance for zero coupler bias, $\Phi_c = 0$.

We approximate the frequencies in the Hamiltonian Eq. (26) as

$$\tilde{\omega}_r \approx \omega_r^p - \frac{K_{0,X}}{2}, \quad \tilde{\omega}_a \approx \omega_a^p - \Xi_a - \frac{K_{0,X}}{2}. \quad (45)$$

Here we omit other interaction-induced shifts that are of order of $g_{\pm}^2/\tilde{\omega}_{r,a}$. Full expressions are provided in Appendix A. Notice the shift proportional to $K_{0,X}$ the main contribution to cross-Kerr coupling strength. Another frequency shift is due to the atom anharmonicity

$$\Xi_a = \frac{E_C^a}{\hbar} \left[\frac{5}{3} \left(\frac{E_L^a}{\tilde{E}_L^a} \right)^2 \left(\phi_a^{\min} - \frac{2\pi\Phi_c}{\Phi_0} \right)^2 - \frac{E_L^a - \tilde{E}_L^a}{\tilde{E}_L^a} \right]. \quad (46)$$

In the brackets, the first term comes from the cubic perturbation in the atom potential. The second one is the quartic correction. See Appendix A for a derivation using the Schrieffer-Wolff transformations. Note that the shift analogous to Ξ_a is negligibly small in the resonator frequency $\tilde{\omega}_r$.

According to Eqs. (45), the resonator and the atom frequencies are $\tilde{\omega}_r \approx 2\pi 6.74$ GHz $- K_{0,X}/2$ and $\tilde{\omega}_a \approx 2\pi 13.49$ GHz $- K_{0,X}/2$. It is already clear that we hit the resonance when $K_{0,X}/2 < \tilde{g}_2$. In fact, calculations

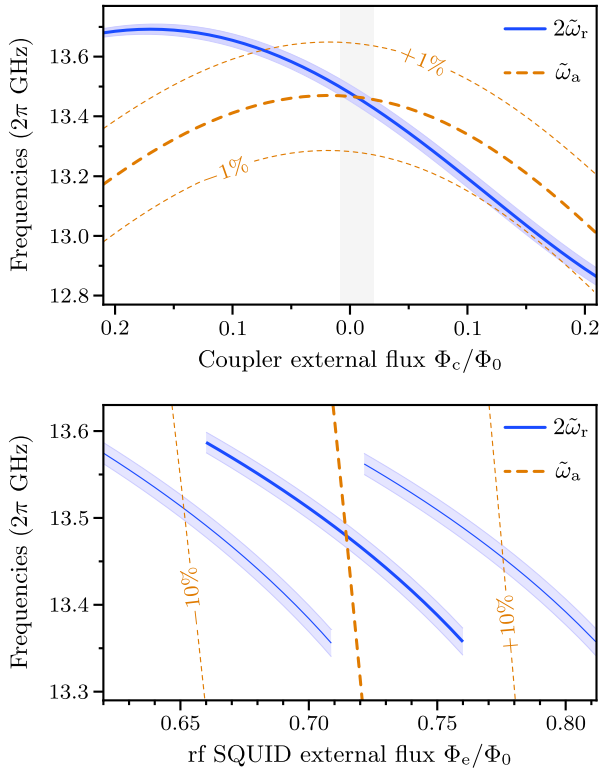


FIG. 5. Dependence of the resonator and atom frequencies on the flux biases: the coupler bias Φ_c in the upper panel and the atom bias Φ_e in the lower panel. Resonator frequency $\tilde{\omega}_r$ according to Eq. (45); atom frequency $\tilde{\omega}_a$ determined numerically as described in the text. Blue area is the region from $2\tilde{\omega}_r - \tilde{g}_2$ to $2\tilde{\omega}_r + \tilde{g}_2$, where \tilde{g}_2 is the two-photon coupling strength. Gray shade marks the minimal region of two-photon resonance, i.e. where the detuning is smaller than \tilde{g}_2 . Circuit parameters as in the text. Thin lines show the frequencies when the atom Josephson energy departs from the required value by the indicated fraction.

yield $K_{0,X} \approx 2\pi 15.7$ MHz and $|\tilde{\omega}_a - 2\tilde{\omega}_r| \approx 2\pi 1.5$ MHz, while $\tilde{g}_2 \approx 2\pi 27.0$ MHz.

Note also that the quartic contribution to the anharmonicity in Eq. (46) provides a correction of order of magnitude of E_C^a/\hbar . More precisely, it is about 30 MHz with the artificial atom parameters as in Sec. V A. This correction exceeds \tilde{g}_2 and hence is important for us.

D. Numerics for the resonance position

Furthermore, we study the resonance position numerically in Fig. 5. The panels there demonstrate how the system frequencies depend on the coupler bias Φ_c and the atom bias Φ_e . To determine the atom frequency in the figure, we solve the Schrödinger equation for the rf SQUID potential [20]

$$U'_a = U_a - E_J^c \cos\left(\phi_r^{\min} - \phi_a - \frac{\pi\Phi_c}{\Phi_0}\right) \quad (47)$$

that is perturbed by the coupler. Here the potential U_a of the uncoupled atom is given by Eq. (44). For $\Phi_c = 0$, the atom frequency is $\tilde{\omega}_a \approx 2\pi 13.47$ GHz $- K_{0,X}/2$. That differs from the analytical prediction by about $2\pi 13$ MHz.

Analytical approximation in Eq. (45) neglects various other interaction-induced shifts. They are much smaller than the two-photon coupling strength \tilde{g}_2 when the latter is close to its maximal value. However, we take into account the influence of the coupler Josephson energy that can be of order of 1 GHz. We have already discussed in Sec. V B how that is required to tune the resonance. On the other hand, this contribution exceeds the overall approximation error in Eqs. (45). Mostly, this error arises as the analytics underestimates the atom anharmonicity (see Sec. V A).

We have verified that, for a smaller number of metastable energy levels, this discrepancy increases. Eventually, this may even prevent reaching the two-photon resonance if the analytics is used to choose the system parameters. According to the Fig. 5 upper panel, even a relatively small decrease in the atom frequency $\tilde{\omega}_a$ can prevent it from crossing the $2\tilde{\omega}_r$ curve. Thus, the resonance can become unreachable if one only changes the coupler bias Φ_c *in situ*.

The resonance can be recovered by further tuning of the system frequencies. We expect the resonator frequency to be fixed in the experiment. On the other hand, the atom transition can be varied *in situ* by changing its flux bias Φ_e . That allows one to recover resonance for a rather wide variation in the atom frequency, as shown in the Fig. 5 lower panel.

Figure 5 also shows how sensitive the resonance is to the variation of the atom Josephson energy E_J^a . Similarly to the above, even a small departure in E_J^a can prevent reaching the resonance if one tunes the coupler bias Φ_c alone. Then again, one can fix that by varying the atom bias Φ_e .

Note that a change in E_J^a also shifts the resonator frequency $\tilde{\omega}_r$ as shown in the Fig. 5 lower panel. That occurs as the atom equilibrium ϕ_a^{\min} shifts according to Eq. (9b), which changes the coupler static phase difference δ . In its turn, that alters the magnitude of the coupler Josephson inductance that loads the resonator [see Eq. (7a)]. Similar shifts are rather small for $\tilde{\omega}_r$ in the upper panel, so we do not plot them there. Still, a similar contribution is present in the $\tilde{\omega}_a$ shift. It arises due to the direct change of E_J^a in Eqs. (7b) and (15) combined with the associated change in ϕ_a^{\min} .

E. Interactions

Figure 6 demonstrates how the interactions discussed in Sec. III depend on the coupler external flux Φ_c . In addition to the trivial modulation of the coupler Josephson energy, Φ_c also alters the symmetry of the Josephson interaction. That is, it regulates the onset of the odd components in the coupling energy, including the two-

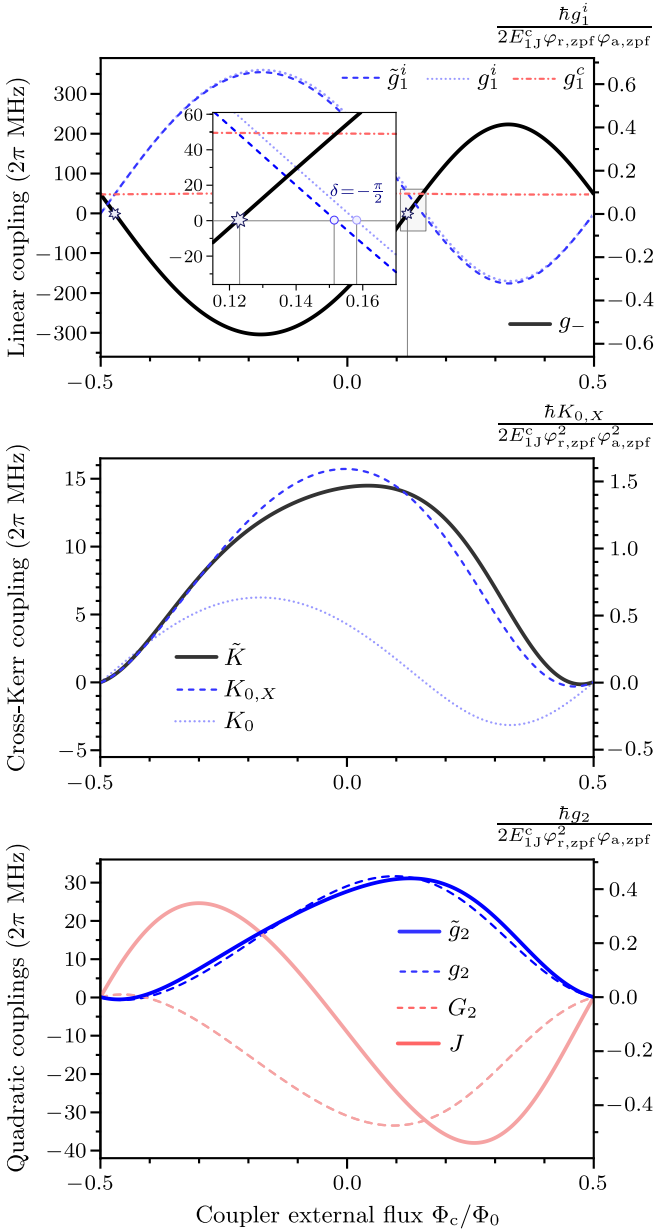


FIG. 6. Dependence of the interaction rates on the coupler bias Φ_c , as expressed in Sec. III. Linear coupling: total inductive \tilde{g}_1^i , bare inductive and capacitive g_1^i and g_1^c , total excitation-number-preserving g_- . The inset shows the vicinity of Φ_c where either g_1^i or \tilde{g}_1^i become zero (circles). Stars mark the biases where g_- vanishes. Cross-Kerr coupling: total \tilde{K} , dressed only by the atom cubic nonlinearity $K_{0,X}$, bare K_0 . Couplings with energies quadratic in the resonator phase: optomechanical J , two-photon bare g_2 , full two-photon \tilde{g}_2 . The coupling quadratic in the artificial atom phase has the rate G_2 . rf SQUID regime as in Fig. 4. Dimensionless axes neglect dependence of the zero-point amplitudes of the resonator and atom, $\varphi_{r,zpf}$ and $\varphi_{a,zpf}$, on the coupler Josephson energy as it varies with Φ_c . The maximal magnitude of the coupler Josephson energy is denoted by $2E_{1J}$.

photon interaction. To obtain the plots, we numerically

solve Eqs. (9a) and (9b) to calculate ϕ_r^{\min} and ϕ_a^{\min} .

The top panel in Fig. 6 shows the single-photon coupling rate g_- given by Eq. (31) along with the two contributions that constitute it: the capacitive coupling g_1^c as in Eq. (19) and the full inductive coupling \tilde{g}_1^i as in Eq. (29). We also plot the bare inductive coupling g_1^i as in Eq. (20). Notice that the capacitive coupling is virtually constant in the coupler bias. That is to be expected, as renormalizations due to the coupler Josephson inductance in Eqs. (7a) and (7b) are negligible for $E_J^c \ll E_L^r, E_L^a$.

By setting $\Phi_c \bmod \Phi_0 = \Phi_0/2$, we turn off the coupler Josephson energy, $E_J^c = 0$. Thus, all linear and nonlinear inductive-type couplings vanish, leaving only the capacitive coupling. On the other hand, bare inductive coupling g_1^i vanishes as Φ_c satisfies $\delta \bmod \pi = \pi/2$, where δ is given by Eq. (8).

The full inductive coupling \tilde{g}_1^i has an additional component due to the asymmetry in the atom potential. With the cubic nonlinearity coefficient $\mu = 1.651$ (for $E_J^c = 0$ and $C'_c = 0$), this component is noticeable in the plot as a difference between \tilde{g}_1^i and g_1^i . As follows from Eq. (29), \tilde{g}_1^i vanishes for the bias determined by the condition $\cot \delta = \frac{5}{6}\mu\varphi_{a,zpf}^2$. This zero-shifting component is proportional to the bare G_2 interaction (see lower panel) and $\sin \delta$. Hence, this component is close to its maximal magnitude right near the zero of the bare coupling g_1^i . Equation (31) suggests an important property: for specific values of the external flux Φ_c , the capacitive and inductive couplings cancel each other out, and the single-photon coupling switches off [49, 63]. We mark these values of Φ_c in Fig. 6.

The middle panel in Fig. 6 demonstrates the cross-Kerr coupling rate \tilde{K} as in Eq. (37). We also plot the bare rate K_0 as in Eq. (21); as follows from the equation, it vanishes for Φ_c at either $\delta \bmod \pi = \pi/2$ or $\Phi_c \bmod \Phi_0 = \Phi_0/2$ analogously to the inductive coupling g_1^i . The plot shows that, for our circuit parameters, the bare cross-Kerr coupling acquires an essential renormalization as in the second term in Eq. (35). Furthermore, we plot the rate $K_{0,X}$ as in Eq. (36) that only takes into account virtual processes due to the atom cubic nonlinearity. For our parameters, it provides the main contribution to the total value of the cross-Kerr coupling rate \tilde{K} . As seen from the plot and according to Eq. (37), the difference $\tilde{K} - K_{0,X}$ is the most pronounced where the linear coupling rate g_- is higher.

The bottom panel in Fig. 6 shows the couplings with the energy quadratic in the atom variables, particularly the sought-after two-photon coupling. The first term in Eq. (43) constitutes the dominating contribution to the total value of the two-photon coupling \tilde{g}_2 . As in the cross-Kerr coupling rate, the further corrections are more pronounced with higher linear coupling strength g_{\pm} . Close to the maximal magnitude of the two-photon coupling, g_{\pm} is vanishing. Therefore, corrections in Eq. (43) are negligible, and $\tilde{g}_2 \approx g_2$ is an excellent approximation.

This implies that the maximal strength of the two-photon coupling \tilde{g}_2 depends roughly linearly on the cou-

pling energy E_j^c according to Eq. (22). On the other hand, the value of E_j^c is bounded by the condition (27). When it does not hold, our perturbative treatment of the off-resonant single-photon coupling breaks down.

Note, that for the unbiased coupling SQUID, the magnitude of the two-photon coupling is only about 11% smaller than at its maximum. Hence, if that is a reasonable tradeoff, a single Josephson junction may be used instead of a coupling SQUID, possibly reducing the amount of noise in the system. In that case, two-photon coupling arises solely due to a non-zero equilibrium phase of the metastable rf SQUID, as discussed in the preceding work [20].

VI. DISCUSSION

We have calculated the rates of some interesting interactions mediated by the coupling SQUID, including their renormalizations from up to three different types of processes. How seriously should we treat these, rather intricate, findings? Here we discuss the bosonic approximation, neglecting some nonlinearities, and coupling to the environment.

A. Commutation relations for the atom operators

a. Bosonic approximation. In determining the cross-Kerr coupling rate, we rely on the bosonic approximation for the artificial atom metastable states. In other words, we assume that the atom does not leave its metastable well as in Fig. 4; while, at the same time, it can be excited arbitrarily high in energy. Clearly, these two assumptions are contradicting for a metastable potential. However, we expect them to hold for the atom phase dwelling sufficiently close to the metastable well minimum.

More precisely, we assess the plausibility of the bosonic approximation by looking into the virtual processes that comprise the corrections. We have found that the main cross-Kerr renormalization in Eq. (36) requires at least four metastable states as shown for a contributing virtual process in Fig. 2(II). Other less important corrections require at most five metastable states to be available: See Fig. 2(II) for a single-photon $|(n+1)g\rangle \leftrightarrow |ne\rangle$ correction as in Eqs. (28)–(29) and Fig. 3(b) for a two-photon $|(n+2)g\rangle \leftrightarrow |ne\rangle$ correction as in Eqs. (43).

However, near the maximum of the two-photon interaction rate, its dominating correction requires only four atom levels as in Figs. 3(a) and (c). This correction is proportional to $\cos\delta$, while the coupler static phase δ modulo π is close to $\pi/2$ near the two-photon maximum. Such a correction is small, as discussed for Eq. (43) and in Sec. V. Still, the one in Fig. 3(b) with five atom levels is even smaller, as it is proportional to $\cos^2\delta$. A similar correction, given by the last term in Eq. (43), is small for a reasonable set of parameters such as in Sec. V.

Note that the situation changes in the practically questionable case of $g_1^c \gtrsim (g_1^i)_{\max}$ with weaker inductive coupling as discussed for Eq. (43). In that case, processes that use five atom levels become relevant in the two-photon correction for any δ .

In any case, all mentioned processes occur well within the seven metastable energy states of the rf SQUID in Sec. V. On the other hand, a process going beyond that occurs differently than predicted by the bosonic approximation. Such real process can bring the system out of the metastable state subspace as the rf SQUID relaxes into the right well in Fig. 4. At the same time, we expect that a virtual process predicted by the bosonic model simply does not occur in that case—if the dissipation into the right well is faster than the interactions that comprise the virtual process.

b. Quasispin approximation as an alternative. Another approach is to cut the Hilbert space to the metastable states right from the start [22, 23]. In this model, any process exciting the atom further above simply does not occur; algebraically, for example, that corresponds to $\sigma_+|u\rangle = 0$ for a system with the highest energy state $|u\rangle$ with the raising operator such as $\sigma_+|g\rangle = |e\rangle$ etc. This model predicts that a real process going above the metastable levels does not occur, although in reality the system can leave the metastable subspace in that case. However, for the calculation of renormalizations due to virtual processes, quasispin approximation may be a better model as it takes into account only the processes within the quasispin subspace. This restriction from above is encoded into the commutation relations $[\sigma_+, \sigma_-] = Z$. Here $\sigma_+ = (X+Y)/2$ and $\sigma_- = (X-Y)/2$ are the raising and lowering operators, where X, Y , and Z are the spin projection operators for the respective axes. In other words, in $\sigma_- \sigma_+ = \sigma_+ \sigma_- - Z$, the state-dependent addition Z on the right-hand side ensures that it vanishes when acting on the highest excited state $|u\rangle$.

We only mention here that our calculations in Appendix A would have become even more tedious in this approach, where the commutator of the ladder operators is operator-valued. As for the question of determining the best model to describe metastable energy states, we leave it for future work. A similar question arises for modeling transmons which can “ionize” due to energetic driving [54, 64].

c. Two-photon coupling. As explained for Eq. (43), the main part of the two-photon coupling rate \tilde{g}_2 typically comes from the bare interaction. That is the case for reasonable linear coupling rates and comparable zero-point fluctuations of the atom and resonator. We have also demonstrated that in the estimates of Sec. V. That confirms our assumption in the preceding work [20], where we claimed it is enough to assess the bare two-photon coupling. Moreover, that suggests that our estimate on attainable magnitudes of the two-photon coupling does not rely on the bosonic approximation.

B. Some neglected nonlinearities

a. Expansion of the Josephson coupling energy. It is possible to find the coefficients for the Hamiltonian terms as in Eqs. (14)–(18) and higher in all orders of the coupling energy expansion [65, 66]. However, we resort to the fourth-order expansion in our starting Hamiltonian. The reason is that we work with a relatively strong Josephson coupling to boost the two-photon processes. Consider the perturbative two-photon corrections in Eq. (43). They are of the same order in the small zero-point fluctuations as the neglected higher-order expansion terms in the coupler potential energy. However, with stronger Josephson coupling, these corrections exceed the higher-order expansion terms and should be accounted for. With the relatively strong Josephson coupling, we need to tackle the higher perturbative corrections as we include the higher expansion terms. That is beyond the scope of this work.

b. Coupling-induced self-nonlinearities. In our results, we retain some influence of the Josephson energy E_J^c of the coupler, unlike the preceding part of this work [20]. It influences the atom and the resonator frequencies as discussed in Sec. VB. The reason is in the plasma frequency dependence on the coupling energy according to Eqs. (16), (17), and (15).

Capacitive coupling as in Eq. (19) depends on E_J^c in the same manner. However, this variation is not so important practically and can be barely seen in the upper panel of Fig. 6. Moreover, we have neglected the coupling-induced nonlinearities compared to the atom self-nonlinearity in the sequences of virtual processes as in Figs. 2 and 3(b). See also the explanations for Eq. (30).

c. Resonator anharmonicity. Due to relatively high values of the coupler Josephson energy, the resonator acquires anharmonicity Ξ_r from the coupler. Its effect on the two-photon resonance is negligible if for n_r photons when $n_r \Xi_r$ is much smaller than the coupling rate \tilde{g}_2 . According to Appendix A 2 c, that is the case for

$$n_r \ll \frac{E_L^r}{2E_C^r} \frac{\varphi_{r,zpf}^2 \varphi_{a,zpf}}{|-\pi/2 - 5E_J^c/3E_L^r - \delta|} \quad (48)$$

when sufficiently detuned from the pole in the right-hand side. For the resonance at zero coupler bias $\Phi_c = 0$ as in Sec. VC, we have $-\pi/2 - \delta \approx -\pi/2 - \phi_a^{\min} \approx -0.1\pi$ according to Eq. (8), Sec. VA, and assuming $\phi_r^{\min} \approx 0$. There, the resonance condition is still unaffected by the induced resonator anharmonicity once $n_r \lesssim 20$. We also estimate that further away from $\delta = -\pi/2 - 5E_J^c/3E_L^r$, the resonator anharmonicity only reaches about $2\pi 4$ MHz. Therefore, we expect our plot of resonator frequency in Fig. 5 to be accurate for a reasonable number of photons.

C. Coupling to environment

a. Dissipation. The neglected squeezing also changes the decay rates, but, again, only negligibly.

Therefore, at least for the weak Markovian dissipation, a standard Heisenberg-Langevin treatment [23, 59, 67–69] can be plugged in, without changing the rest of our reasoning.

It may seem that an issue arises, if both the resonator and the artificial atom couple to the same or correlated heat baths. That yields an additional linear coupling between them [70, 71]. As follows from Eqs. (43) and (37), the two-photon and the cross-Kerr coupling rates renormalize as well, as they depend on the linear coupling strength. However, all these contributions are small in the strong coupling regime, where the interactions are faster than the dissipation. Hence we believe that our quantitative theory of the coupling rates still holds.

In addition, it is known that dissipation renormalizes the resonance frequencies [23, 72]. At this point, it is natural to assume that the coupling SQUID does not mediate a substantial coupling to the environment. In that case, both the dissipation and the respective renormalization of the resonances do not depend on the coupler bias. This renormalization is then of little concern for us.

b. Quantumness. The corrections as calculated for the interactions in Eqs. (29), (34), (37), and (43) are genuinely quantum. They arise owing to interactions with the zero-point fluctuations, as signified by the vacuum loops in Figs. 2 and 3. Are these corrections still present after interactions with the environment?

Mathematically, they arise due to the noncommutativity of the atom operators. With no atom-resonator coupling, it follows from the Heisenberg-Langevin treatment in the rotating-wave and Markov approximations, that

$$b(t) = b(0)e^{-i\omega_a t - \frac{\gamma}{2}t} - i\sqrt{\frac{\gamma}{2\pi}} \int_0^t dt' \int_0^\infty d\omega e^{-(i\omega_a + \frac{\gamma}{2})(t-t')} c_\omega(0) e^{-i\omega t'}, \quad (49)$$

where c_ω is the annihilation operator of a bath boson in a mode of frequency ω_k , and γ denotes the atom damping rate. The second part of this expression assures [67] that the commutator $[b, b^\dagger] = 1$ holds at any time t .

However, quantum coherence should not vanish faster than one is able to measure the related frequency shift. In simpler terms, the frequency shift should overcome the dephasing rate in the system. To assess when that is possible, one may conduct the estimates similar to Ref. [73], where the applicability of classical approximation was discussed. However, to observe quantum effects, the measurement should be much faster than the system decay. Hence the dephasing rates due to fluctuations in the coupled system should be found in the limit of the long-living coupled system [74]. We leave that for future work.

In addition, the calculated corrections can be screened with thermal occupancy. This can be seen from the expression $\langle bb^\dagger \rangle = n_a^{\text{th}} + 1$ for the atom populated with $n_a^{\text{th}} = \langle b^\dagger b \rangle$ thermal excitations alone. Hence, to clearly

observe the *quantum* corrections to the interactions, thermal occupancy should be negligible with $n_a^{\text{th}} \ll 1$. This very condition is typically sought for in the experiments in circuit quantum electrodynamics.

VII. OUTLOOK

a. Photodetection. We have confirmed our estimate as in the preceding part [20]: a sizeable two-photon coupling can arise between a resonator and an rf SQUID. First of all, it is tempting to study its use for detection of photon pairs. In that case, the rf SQUID can act as a Josephson photomultiplier [31–34]. In some works [22, 29, 30, 75], the excited metastable state of the device tunnels immediately on absorption. Then, to achieve high tunneling rates, the excited state may lay close to the barrier top, while the states above and on the other side of the barrier are extremely dissipative. With only two relatively coherent metastable states, our bosonic approximation will break as discussed in Sec. VI. We expect the theory as in Refs. [22, 23] to be more appropriate in that case.

b. Other systems to couple. Our theory can be used to characterize the two-photon and cross-Kerr interactions between a resonator and some other types of artificial atoms apart from the flux-biased phase qubit.

Current-biased phase qubit [76] have similar potential and level structure in the relevant region of phases, hence we expect that our theory translates for it directly. However, its equilibrium phase is, approximately, a multiple of π . Hence to achieve two-photon coupling between a resonator and a current-based phase qubit, one can additionally bias the symmetrical SQUID. However, that yields suboptimal coupling rates similarly to the transmon case discussed in the preceding part [20] of our work.

Another qubit type, flux qubit [77], is highly anharmonic. Strictly speaking, our calculation for the artificial atom as an anharmonic oscillator does not hold in that case. However, as noted in the preceding work [20], two-photon coupling rate is still expressed with a similar formula. We expect that it attains comparable magnitudes for the flux qubit. On the other hand, we expect no cross-Kerr renormalization as in Eq. (35). Virtual transitions that inhibit it are suppressed by the high frequency mismatch between the first and the second transition in flux qubit. However, the cross-Kerr corrections due to the linear interactions in Eqs. (38) are valid in the flux-qubit limit of $-\bar{\varepsilon}_a \gg \tilde{\omega}_a$. These corrections, while small for the phase qubit, become dominant for the flux qubit. The nonlinear corrections in Eqs. (39) and (41) should be extended to cover the high-anharmonicity case. Same considers the last two corrections in Eq. (43) for the two-photon coupling.

As for the transmon, using an asymmetrical SQUID coupler [19, 24] may be advantageous [20]. Besides that, our theory for renormalized interactions should be slightly modified. Having a symmetrical potential, trans-

mon only acquires a cubic nonlinearity from the coupler SQUID. It is then comparable to the resonator cubic nonlinearity X_r in Eq. (17) of the same origin, which is negligible in the coupling rates we have calculated. Then, when the atom cubic nonlinearity X_a is also vanishing, there are no renormalizations in the cross-Kerr and linear inductive couplings as given in Eqs. (29) and (36). However, such induced cubic nonlinearities may contribute with higher Josephson energies of the coupler. Then both of them matter in the coupling renormalizations.

The above reasoning also applies for the coupling of two *LC* oscillators or two resonator modes. We speculated on possible applications for such coupling in the preceding part [20].

c. Cross-Kerr coupling for applications. In addition to the two-photon coupling, the SQUID coupler provides a sizeable cross-Kerr interaction, as discussed in Sec. V and Ref. [63]. At the same time, similarly to the reference, we can suppress the single-photon coupling. As a result, such a purely cross-Kerr interaction between a transmon and a resonator can be used for qubit read-out [78]. Our theory can be useful for assessing this and other [49, 63] applications. A modification might be required to take into account additional renormalizations if the two-photon coupling is off-resonant.

d. Other interactions. Our theory also allows calculating optomechanical coupling, even if with some modifications. Such a coupling can be used for radiative cooling [52] of an artificial atom, as well as for amplification or sensing. In the relevant applications, two-photon coupling would be nonresonant. In that case, it additionally renormalizes the optomechanical coupling as given in Eqs. (33) and (34)—unlike the opposite situation that we have considered in this work. Other interactions renormalize the optomechanical coupling as well; in fact, if one is interested in these corrections, the calculations in Appendix A 2 should be redone with the roles of the two-photon and optomechanical interactions reversed. Still, we expect that these corrections are minor as they are in our result for the two-photon coupling in Eq. (43).

VIII. CONCLUSIONS

We have considered a resonator and an rf SQUID which interact through a flux-biased dc SQUID. We have obtained expressions for the linear, two-photon, and cross-Kerr coupling rates that include various renormalizations. Using these expressions, we estimate the rates. Our analytical theory can be modified for other applications. With it, we are able to elucidate the origins of the renormalizations and advance understanding of the related approximations.

For a relatively shallow metastable well of an rf SQUID, its cubic nonlinearity provides the main contribution to the renormalizations. For the cross-Kerr and optomechanical interactions, this contribution can be comparable to or even exceed the bare coupling

strength, as seen in Fig. 6. As for the interaction-induced renormalizations, they can become important in other regimes, for example when the single-photon coupling is stronger and less detuned. That is the case for the well-known dispersive contribution in the cross-Kerr coupling in Eq. (37) and the similar renormalizations in the two-photon interaction in Eq. (43). In the latter, such contributions are especially small when the two-photon coupling rate is near its maximal value with respect to variation of the coupling SQUID flux bias. Despite being small, they can still be well in the accuracy of our expansion of the Josephson coupling energy, as discussed in Sec. VI B.

We have discussed validity of our theory in Sec. VI. Most importantly, we have used the bosonic approximation, i.e. we model the artificial atom as an anharmonic oscillator near its metastable minimum. Our results on the *renormalizations* depend on that model validity. Given that fact, does our theory provide quantitatively correct predictions for the renormalizations? We believe that only further numerical or experimental studies can yield a definite answer. However, we have verified that the virtual processes that yield important corrections excite the atom at most to the fourth excited metastable state. Hence we believe that our theory should hold reasonably well for a phase qubit with seven metastable states. For that case, we have provided our theory predictions as described above.

For the numerical estimates, we have focused on the phase qubit regime of the rf SQUID. We fully determine a realistic set of circuit parameters for the setup. Knowing how the interactions renormalize, we choose higher values for the Josephson coupling energy. With that, we assess that the two-photon coupling rate up to almost 30 MHz is feasible, which is about 50% higher than in our preceding work [20]. The cross-Kerr coupling then reaches almost 15 MHz.

If such amount of the cross-Kerr coupling is tolerable, our coupler may be favorable to more complex ones, such as SNAIL [55, 79], by the fact that it requires less junctions. That is especially true when it can be simplified further into a single junction as discussed in Sec. V E.

Finally, we highlight one auxiliary result on the Schrieffer-Wolff transformation to approximately eliminate the cubic perturbation in the potential. While this transformation is known in the literature [55, 80], we rewrite it in terms of dimensionless coordinate and momentum in Eq. (B1). That simplifies manual calculation for Hamiltonians with the interaction terms expressed directly in terms of coordinates and momenta as, for example, used in Refs. [57, 81].

ACKNOWLEDGMENTS

We thank F. Wilhelm-Mauch, A. Semenov, and R. Baskov for discussions and useful comments. E. V. S. acknowledges support from the National Research Foun-

dation of Ukraine through the project No. 2023.03/0165, Quantum correlations of electromagnetic radiation. A. M. S. acknowledges partial support from the Academy of Finland (Contract No. 321982) and the President of Ukraine scholarship for young scientists.

Appendix A: Derivation of the renormalized two-photon Hamiltonian

In this appendix, we reduce the approximate circuit Hamiltonian in Eqs. (1), (13), (14), and (18) to a variation of the two-photon Jaynes-Cummings model where the artificial atom is modeled as an anharmonic oscillator. First, we show how the nonlinear character of the atom potential spawns cross-Kerr interaction. Then, we calculate the relevant renormalizations that originate from the non-resonant interactions.

1. Self-nonlinearity as a perturbation

We start with treating the cubic and quartic nonlinearities of Eqs. (13) and (14) as a perturbation. We approximately diagonalize the atom Hamiltonian $\hat{\mathcal{H}}_a$ in Eq. (14) using a Schrieffer-Wolff transformation [11, 56, 82], $\hat{\mathcal{H}}_a \rightarrow e^{-\Lambda_a \mathcal{S}_a} \hat{\mathcal{H}}_a e^{\Lambda_a \mathcal{S}_a}$, where

$$\Lambda_a = \frac{X_a}{\omega_a^p}. \quad (\text{A1})$$

The anti-Hermitian operator \mathcal{S}_a is given by [55, 80]

$$\mathcal{S}_a = \frac{1}{3}(b^{\dagger 3} - b^3) + 3(b^{\dagger 2}b - b^\dagger b^2) + 3(b^\dagger - b). \quad (\text{A2})$$

For manual calculations, one may rewrite \mathcal{S}_a in terms of $b^\dagger \pm b$ as given in Appendix B. Here, we use the form as in Eq. (A2) and perform the tedious calculations with the computer algebra package QUANTUMALGEBRA.JL [83].

Using the Baker-Campbell-Hausdorff (BCH) formula up to the second commutator,

$$e^{-\Lambda_a \mathcal{S}_a} \hat{\mathcal{H}}_a e^{\Lambda_a \mathcal{S}_a} \approx \hat{\mathcal{H}}_a + \Lambda_a [\hat{\mathcal{H}}_a, \mathcal{S}_a] + \frac{\Lambda_a^2}{2} [[\hat{\mathcal{H}}_a, \mathcal{S}_a], \mathcal{S}_a], \quad (\text{A3})$$

we arrive at the Hamiltonian of a quantum anharmonic oscillator,

$$\frac{\hat{\mathcal{H}}_a}{\hbar} \approx \omega_a^p b^\dagger b - \Xi_a b^\dagger b - \frac{\Xi_a}{2} b^{\dagger 2} b^2 + \omega_a^{\text{zpf}}, \quad (\text{A4})$$

up to the first order in Λ_a . Here $\Xi_a = 60\Lambda_a X_a + 12Y_a$ denotes anharmonicity in the artificial atom energy levels and $\omega_a^{\text{zpf}} = \omega_a^p/2 - 11X_a^2/\omega_a^p - 3Y_a$ is its zero-point energy in the frequency units. The first term in the expression for anharmonicity comes from the cubic perturbation in the Hamiltonian Eq. (14), while the second term comes from the quartic one. In fact, the quartic term is due

to the bare self-Kerr nonlinearity. Using Eq. (16) along with Eqs. (7b), (9b), and the definition of $\varphi_{a,\text{zpf}}$ yields

$$\Xi_a = \frac{E_C^a}{\hbar} \left[\frac{5}{3} \left(\frac{E_L^a}{\tilde{E}_L^a} \right)^2 \left(\phi_a^{\min} - \frac{2\pi\Phi_e}{\Phi_0} \right)^2 - \frac{E_L^a - \tilde{E}_L^a}{\tilde{E}_L^a} \right]. \quad (\text{A5})$$

For deriving Eq. (A4), we have assumed that the cubic nonlinearity in the artificial atom is small with $|\Lambda_a| \ll 1$. Apart from its definition Eq. (A1), another way to express this small parameter is

$$\Lambda_a = \frac{1}{12} \mu \varphi_{a,\text{zpf}}, \quad (\text{A6})$$

where $|\mu| \lesssim 2E_J^a/\tilde{E}_L^a$ according to Eq. (30) for $E_J^c \lesssim E_J^a$. Hamiltonian (A4) with the expression for anharmonicity predict the same corrections to the energy levels as the textbook calculation in Ref. [84].

In the Hamiltonian in Eq. (A4), we have dropped off-diagonal terms of two kinds: One is proportional to $\Lambda_a X_a (b^{\dagger m} b^n + b^{\dagger n} b^m)$, where $m+n$ is even and $2 \leq m+n \leq 4$. Another one is proportional to $\Lambda_a Y_a (b^{\dagger m} b^n + b^{\dagger n} b^m)$, where $m+n$ is odd and $1 \leq m+n \leq 5$. For both types, $m, n = 0, 1, 2, \dots$ and $m \neq n$. Eliminating such terms with a Schrieffer-Wolff transformation yields corrections to the atom frequency and anharmonicity proportional to $\Lambda_a^3 X_a / (m-n)$ and $\Lambda_a^3 Y_a / (m-n)$ that are beyond the accuracy of Eq. (A3). Moreover, according to Eq. (A6), that is far beyond the accuracy of our fourth-order expansion of the Josephson coupling energy [20] in Eq. (18).

Analogously, we apply a Schrieffer-Wolff transformation to the resonator Hamiltonian: $\hat{\mathcal{H}}_r \rightarrow e^{-\Lambda_r \mathcal{S}_r} \hat{\mathcal{H}}_r e^{\Lambda_r \mathcal{S}_r}$, where Λ_r reads as

$$\Lambda_r = \frac{X_r}{\omega_r^p}. \quad (\text{A7})$$

Note that $|\Lambda_r| \ll 1$: the resonator cubic nonlinearity is vanishingly small, as its only source is the SQUID coupler. The operator \mathcal{S}_r is obtained by replacing the atom operators with the resonator ones in Eq. (A2). With the same approximations as in Eq. (A4), we arrive at

$$\frac{\hat{\mathcal{H}}_r}{\hbar} \approx \omega_r^p a^\dagger a - \Xi_r a^\dagger a - \frac{\Xi_r}{2} a^{\dagger 2} a^2 + \omega_r^{\text{zpf}}, \quad (\text{A8})$$

where $\Xi_r = 60\Lambda_r X_r + 12Y_r$ is the resonator anharmonicity and $\omega_r^{\text{zpf}} = \omega_r^p/2 - 11X_r^2/\omega_r^p - 3Y_r$ is its zero-point energy in the frequency units. We further transform the anharmonicity as

$$\Xi_r = \frac{E_C^r}{\hbar} \left[\frac{5}{3} \left(\frac{E_L^r}{\tilde{E}_L^r} \phi_r^{\min} \right)^2 - \frac{E_L^r - \tilde{E}_L^r}{\tilde{E}_L^r} \right], \quad (\text{A9})$$

where we have used Eqs. (17), (7a), (9a), and the definition of $\varphi_{r,\text{zpf}}$. For a small E_J^c/E_L^r , we mention that $\phi_r^{\min} \sim E_J^c/E_L^r$ according to Eq. (9a). That allows us to

obtain the leading terms in Eq. (A9),

$$\Xi_r \approx \frac{E_C^r}{\hbar} \left[\frac{5}{3} \left(\frac{E_J^c}{E_L^r} \right)^2 \sin^2 \delta + \frac{E_J^c}{E_L^r} \cos \delta \right], \quad (\text{A10})$$

where we have used Eq. (7a).

To arrive at the full system Hamiltonian, one also applies the above Schrieffer-Wolff transformations to the rest of the Hamiltonian in Eqs. (1), (13), (14), and (18). After rearrangement, it reads

$$\frac{\hat{\mathcal{H}}}{\hbar} \approx \omega_r a^\dagger a - \frac{\Xi_r}{2} a^{\dagger 2} a^2 + \omega_a b^\dagger b - \frac{\Xi_a}{2} b^{\dagger 2} b^2 + \frac{\hat{\mathcal{H}}_I}{\hbar} \quad (\text{A11})$$

up to the zero-point energy. Here, $\omega_r = \omega_r^p - \Xi_r - K_{0,X}/2$ and $\omega_a = \omega_a^p - \Xi_a - K_{0,X}/2$ denote the resonator and the atom frequencies with

$$K_{0,X} \approx K_0 + 24\Lambda_a g_2. \quad (\text{A12})$$

We have dropped the symmetrical correction of $24\Lambda_r G_2$. That is always possible when the resonator cubic nonlinearity is much weaker than in the atom, i.e. when $|\Lambda_r| \ll |\Lambda_a|$; and when, at the same time, $|g_2| \sim |G_2|$. The latter is true when the vacuum fluctuations in the resonator and the artificial atom $\varphi_{r,\text{zpf}} \sim \varphi_{a,\text{zpf}}$ are comparable. A more general criterion for the approximation in Eq. (A12) to hold, $(E_L^a/E_J^a + \cot \phi_a^{\min}) \sin \delta \lesssim 1$, is obtained by taking into account the condition (27) of no ultrastrong coupling. Using the definition of Λ_a in Eq. (A1) along with Eqs. (16) and (22) in the above expression for $K_{0,X}$, one obtains Eq. (36) in Sec. IV D.

In Eq. (A11), the Hamiltonian $\hat{\mathcal{H}}_I$ aggregates all interaction terms; as it is cumbersome, we do not present it. However, by proper adjustment of the resonator and the atom frequencies, one can make their two-photon coupling dominant. Most of other couplings then act as perturbations and renormalize the dominant interactions.

2. Two-photon regime

With $\omega_a \approx 2\omega_r$, which is close to the two-photon resonance, the interaction Hamiltonian becomes

$$\frac{\hat{\mathcal{H}}_I}{\hbar} \approx -g_2 (a^{\dagger 2} b + b^\dagger a^2) - K_{0,X} a^\dagger a b^\dagger b + \frac{\delta \hat{\mathcal{H}}_I}{\hbar}. \quad (\text{A13})$$

The first two terms here correspond to the dominant interactions: the bare two-photon coupling of strength g_2 and the cross-Kerr coupling of strength $K_{0,X}$ as given by Eq. (A12). Below, we calculate the essential renormalizations to these couplings.

Other interaction terms in the Hamiltonian (A13) are

small or nonresonant. We collect them in its last term,

$$\begin{aligned} \frac{\delta\hat{\mathcal{H}}_I}{\hbar} \approx & -g_-(a^\dagger b + b^\dagger a) - g_+(a^\dagger b^\dagger + ba) \\ & - F(a^\dagger b^\dagger b^2 + b^{\dagger 2} b a) - F(a^\dagger b^{\dagger 2} b + b^\dagger b^2 a) \\ & - g_2(2a^\dagger a + 1)(b^\dagger + b) - J(2b^\dagger b + 1)(a^\dagger + a) \\ & - g_2(a^{\dagger 2} b^\dagger + a^2 b) \\ & - \tilde{G}_2^-(a^\dagger b^2 + b^{\dagger 2} a) - \tilde{G}_2^+(a^\dagger b^{\dagger 2} + b^2 a). \end{aligned} \quad (\text{A14})$$

We treat $\delta\hat{\mathcal{H}}_I$ as a perturbation in Sec. A 2 a. Before, we describe its terms and explain the approximations in it.

The first two terms in the perturbation Hamiltonian Eq. (A14) correspond to the number-conserving and number-nonconserving parts of the linear interaction as described in Sec. IV B. Their coupling rates $g_\pm = g_1^c \pm \tilde{g}_1^i$ include contributions from both capacitive and inductive couplings. The latter coupling strength renormalizes as

$$\tilde{g}_1^i \approx g_1^i + 20\Lambda_a G_2, \quad (\text{A15})$$

where we neglect a contribution of $3(g_3 + G_3)$ from the fourth-order expansion term in the coupler Josephson energy. Indeed, when $E_C^r \ll \tilde{E}_L^r$ and $E_C^a \ll \tilde{E}_L^a$, the relevant vacuum fluctuations are small with $\varphi_{r,\text{zpf}}^2, \varphi_{a,\text{zpf}}^2 \ll 1$. Thus, $3|g_3 + G_3| \ll |g_1^i|$ as follows from Eqs. (20), (23), and (25). As for the second term in Eq. (A15), it matters near the points $\delta \bmod \pi = \pi/2$ where the bare inductive coupling g_1^i vanishes.

Away from it, the entire renormalization of the linear coupling g_1^i often can be negligible. The coupling strength G_2 is of higher order in the vacuum fluctuations compared to g_1^i . Thus, we have that $20\Lambda_a|G_2| \ll |g_1^i|$ as far as $\mu\varphi_{a,\text{zpf}}^2 |\tan \delta| \ll 1$. In that case, $\tilde{g}_1^i \approx g_1^i$ according to Eq. (A15).

The second line in Eq. (A14) describes couplings with the energy cubic in the atom variables. These couplings have the renormalized (see Sec. IV D) rate

$$F = 3G_3 + 20\Lambda_a G_2 \quad (\text{A16})$$

and cause a single-excitation exchange between the resonator and atom, as well as their simultaneous excitation or de-excitation by one energy level. However, unlike the linear interactions in the first line of Eq. (A14), excitation and de-excitation of the atom occur in two steps here. During the excitation, the atom first goes two energy levels up, and then one level down. The process proceeds in reverse during the de-excitation. Up to the order of creation and annihilation processes, this interaction is a linear coupling with its strength modulated by the atom occupancy $b^\dagger b$.

The third line in Eq. (A14) describes the couplings of optomechanical type. One of them has its strength renormalized as

$$J = G_2 + 6\Lambda_a g_1^i. \quad (\text{A17})$$

Plugging Eqs. (20), (24), and (A1) into the above expression and using Eq. (9b) yields Eq. (34) in Sec. III.

The penultimate line in Eq. (A14) represents the non-resonant coupling with its energy quadratic in the resonator variable. This coupling of the rate g_2 leads to simultaneous excitation or de-excitation of the resonator by one energy level and the atom by two energy levels.

The last line in Eq. (A14) contains coupling energies quadratic in the atom variables. The first term therein describes the coupling of the rate \tilde{G}_2^- that induces annihilation of one resonator photon and excitation of the atom by two energy levels, and vice versa. The second term describes the coupling of the rate \tilde{G}_2^+ leading to simultaneous excitation or de-excitation of the resonator by one energy level and the atom by two energy levels. The rates of these couplings are determined as

$$\tilde{G}_2^\pm = G_2 - 2\Lambda_a(g_1^i \pm 2g_1^c). \quad (\text{A18})$$

Here the first term comes from the bare coupling in the Hamiltonian Eq. (18) and the second one is a renormalization as described in Sec. IV D.

In $\delta\hat{\mathcal{H}}_I$ in Eq. (A14), we have retained only the terms that provide essential renormalizations. In fact, dressing the couplings in Eq. (18) with the atom cubic nonlinearity—in addition to renormalizing them—also creates new couplings different from those in the bare interaction Hamiltonian (18). However, they are of comparable magnitudes as the same-type terms that we neglect in the cosine expansion [20] of the coupler Josephson energy in Eq. (18). In other words, we omit these new couplings in Eq. (A14) as they exceed the accuracy of our approximation in the Hamiltonian Eq. (18).

In addition to the negligible new couplings, small coupling terms of the same type as in the Hamiltonian Eq. (18) also arise in Eq. (A13). They read as

$$\begin{aligned} \frac{\delta\hat{\mathcal{H}}_I}{\hbar} = & -\tilde{G}_3(a^\dagger + a)(b^{\dagger 3} + b^3) \\ & -g_3(a^{\dagger 3} + a^3)(b^\dagger + b) \\ & -\frac{\tilde{K}_0}{4}(a^\dagger + a)^2(b^{\dagger 2} + b^2) \\ & -\frac{K_{0,X}}{4}(2b^\dagger b + 1)(a^{\dagger 2} + a^2) \end{aligned} \quad (\text{A19})$$

with $\tilde{G}_3 = G_3 - 4\Lambda_a G_2$ and $\tilde{K}_0 = K_0 - 8\Lambda_a g_2$. These terms yield only negligible corrections to the frequencies and to the cross-Kerr and two-photon interaction rates. We have verified that such corrections appear at least in the seventh order in the zero-point fluctuations $\varphi_{r,\text{zpf}}$ and $\varphi_{a,\text{zpf}}$ and are beyond the accuracy of our expressions. Note that in Eqs. (A14) and (A19), we account for the corrections to the coupling rates proportional to Λ_a while neglecting the corrections proportional to Λ_r since $|\Lambda_r| \ll |\Lambda_a|$.

a. Elimination of nonresonant linear and optomechanical interactions

The perturbation $\delta\hat{\mathcal{H}}_1$ can be approximately eliminated via the Schrieffer-Wolff transformation $\hat{\mathcal{H}} \rightarrow e^{-\mathcal{W}}\hat{\mathcal{H}}e^{\mathcal{W}}$, where the anti-Hermitian operator \mathcal{W} reads as

$$\begin{aligned} \mathcal{W} = & \lambda_-(a^\dagger b - b^\dagger a) + \lambda_+(a^\dagger b^\dagger - ba) \\ & + \zeta_-(b^{\dagger 2}ba - a^\dagger b^\dagger b^2) + \zeta_+(a^\dagger b^{\dagger 2}b - b^\dagger b^2 a) \\ & + \lambda_r(a^\dagger a + \frac{1}{2})(b - b^\dagger) + \lambda_a(b^\dagger b + \frac{1}{2})(a - a^\dagger) \\ & + \lambda_2(a^{\dagger 2}b^\dagger - ba^2) \\ & + \eta_+(a^\dagger b^{\dagger 2} - b^2 a) + \eta_-(b^{\dagger 2}a - a^\dagger b^2). \end{aligned} \quad (\text{A20})$$

The parameters $\lambda_\pm, \lambda_r, \lambda_a, \lambda_2, \zeta_\pm, \eta_\pm \ll 1$ are defined as

$$\begin{aligned} \lambda_\pm &= \frac{g_\pm}{\omega_a \pm \omega_r}, \quad \zeta_\pm = \frac{F}{\omega_a \pm \omega_r - \Xi_a}, \\ \lambda_r &= -\frac{2g_2}{\omega_a}, \quad \lambda_a = -\frac{2J}{\omega_r}, \quad \lambda_2 = \frac{g_2}{\omega_a + 2\omega_r}, \\ \eta_\pm &= \frac{\tilde{G}_2^\pm}{2\omega_a \pm \omega_r - \Xi_a}. \end{aligned} \quad (\text{A21})$$

Now we use the approximate BCH formula as for Eqs. (A4) and (A8). With the operator \mathcal{W} and the Hamiltonian (A11), that yields

$$\begin{aligned} \frac{\hat{\mathcal{H}}}{\hbar} \approx & \tilde{\omega}_r a^\dagger a - \frac{\tilde{\Xi}_r}{2} a^{\dagger 2} a^2 + \omega'_a b^\dagger b - \frac{\Xi'_a}{2} b^{\dagger 2} b^2 \\ & - K' a^\dagger a b^\dagger b - \tilde{g}_2 (a^{\dagger 2} b + b^\dagger a^2) + \frac{\delta\hat{\mathcal{H}}'_1}{\hbar}. \end{aligned} \quad (\text{A22})$$

Here $\delta\hat{\mathcal{H}}'_1$ is the perturbation term aggregating all non-resonant couplings. For deriving Eq. (A22) we have used that $\hat{\mathcal{H}}_1$ is given by Eqs. (A13) and (A14). In Eq. (A22), we have omitted the higher-order nonlinearities exceeding the accuracy of approximation in Eqs. (13) and (14).

Consider the renormalizations due to the perturbation $\delta\hat{\mathcal{H}}_1$. The resonator frequency is renormalized as

$$\begin{aligned} \tilde{\omega}_r = & \omega_r - \lambda_- g_- - \lambda_+ g_+ + 2(2\lambda_r - \lambda_2)g_2 \\ & - 2(\lambda_2 g_2 + \eta_+ \tilde{G}_2^+ + \eta_- \tilde{G}_2^-), \end{aligned} \quad (\text{A23})$$

while its self-Kerr anharmonicity becomes

$$\tilde{\Xi}_r = \Xi_r - 2(2\lambda_r - \lambda_2)g_2. \quad (\text{A24})$$

The renormalized atom frequency reads

$$\begin{aligned} \omega'_a = & \omega_a + \lambda_- g_- - \lambda_+ g_+ + 4\lambda_a J - 2\lambda_2 g_2 \\ & - 2(\zeta_+ g_+ + \lambda_+ F + \eta_+ \tilde{G}_2^+) - 2\lambda_+^2 \Xi_a. \end{aligned} \quad (\text{A25})$$

We also calculate the renormalized atom anharmonicity,

$$\begin{aligned} \Xi'_a = & [1 + 2(\lambda_+^2 - \lambda_-^2 + 2\lambda_2^2)]\Xi_a \\ & - 4\lambda_a J + 2(\eta_+ \tilde{G}_2^+ - \eta_- \tilde{G}_2^-). \end{aligned} \quad (\text{A26})$$

However, we assume that it renormalizes only negligibly, $\Xi'_a \approx \Xi_a$. We have verified this assumption for the parameters provided in Sec. V. Note that in Eqs. (A23)–(A26), we retain only the corrections that are within the accuracy of the interaction Hamiltonian in Eq. (18).

The cross-Kerr coupling gets dressed further by the nonresonant interactions in the Hamiltonian (A14) and its strength becomes

$$\begin{aligned} K' = & K_{0,X} + 2(\lambda_-^2 + \lambda_+^2)\Xi_a \\ & + 2(\zeta_+ g_+ - \zeta_- g_-) + 2(\lambda_+ - \lambda_-)F \\ & + 4(\lambda_2 g_2 + \eta_+ \tilde{G}_2^+ + \eta_- \tilde{G}_2^-) \\ & + 4(\lambda_r^2 + 2\lambda_2^2 + 4\eta_+^2 + 4\eta_-^2)\Xi_a. \end{aligned} \quad (\text{A27})$$

The part of the coupling strength $K_{0,X}$ is given by Eq. (A12), where it is already dressed due to the diagonalization of the uncoupled artificial atom and the resonator Hamiltonians. In Eq. (A27), the terms of the second order in the small parameters contribute significantly when $|\Xi_a| \gg |K_{0,X}|$.

In Eq. (A27), we drop the term $2(\zeta_+ + \zeta_-)F$ as it is of the eighth order in the zero-point fluctuations $\varphi_{r,zpf}$ and $\varphi_{a,zpf}$. Thus, it is beyond the accuracy of the interaction Hamiltonian in Eq. (18). For the same reason, we also neglect the term $2(\zeta_+^2 + \zeta_-^2)\Xi_a$ assuming that $|\Xi_a| \ll \omega_r, \omega_a$.

Finally, we provide the renormalized two-photon coupling strength,

$$\tilde{g}_2 = g_2 + \frac{\lambda_a}{2}g_- - \lambda_- J + \eta_- g_+ + \lambda_+ \tilde{G}_2^-. \quad (\text{A28})$$

Here, we have dropped the correction $\zeta_+ \tilde{G}_2^- + \eta_- F$ as it is of the sixth order in the zero-point fluctuations $\varphi_{r,zpf}$ and $\varphi_{a,zpf}$ and hence beyond the accuracy of the Hamiltonian in Eq. (18). Using Eq. (A21) in Eq. (A28), assuming that $|\Xi_a| \ll \omega_a$, and recalling that we are in the two-photon regime with $\omega_a \approx 2\omega_r$, one obtains Eq. (43) in Sec. IV. We leave the terms of the fifth order in $\varphi_{r,zpf}$ and $\varphi_{a,zpf}$, as they may be relevant as explained in the main text.

b. Elimination of nonresonant higher-order interactions

The perturbation term in the Hamiltonian (A22) further renormalizes the resonances and the dominant couplings. It reads

$$\frac{\delta\hat{\mathcal{H}}'_1}{\hbar} \approx \lambda_- \Xi_a (a^\dagger b^\dagger b^2 + b^{\dagger 2} ba) - \lambda_+ \Xi_a (a^\dagger b^{\dagger 2} b + b^\dagger b^2 a). \quad (\text{A29})$$

This perturbation arises as the nonresonant linear interactions in Eq. (A14) dress the atom anharmonicity term in the Hamiltonian (A22). Notice that it contains the couplings of the same type as in the second line of Eq. (A14). The Hamiltonian in Eq. (A29) is nonnegligible for $|\Xi_a| \gg |F|$. In this case, magnitudes of the couplings in Eq. (A29) are comparable to the rate F of the

similar couplings in the Hamiltonian in Eq. (A14). Hence their contributions to the renormalizations are comparable too.

In Eq. (A29), we neglect the terms spawned as the *non-linear* couplings from Eq. (A14) dress the atom anharmonicity term in the Hamiltonian (A22). We assume that for relatively weak atom anharmonicity, $|\Xi_a| \ll \omega_r, \omega_a$, these terms provide negligible contributions to the renormalizations.

We eliminate $\delta\hat{\mathcal{H}}'_1$ in the Hamiltonian (A22) using the Schrieffer-Wolff transformation $\hat{\mathcal{H}} \rightarrow e^{-\mathcal{W}'} \hat{\mathcal{H}} e^{\mathcal{W}'}$ with

$$\mathcal{W}' = \lambda'_-(a^\dagger b^\dagger b^2 - b^{\dagger 2} b a) + \lambda'_+(a^\dagger b^{\dagger 2} b - b^\dagger b^2 a). \quad (\text{A30})$$

Here the parameters $\lambda'_\pm \ll 1$ are given by

$$\lambda'_\pm = \lambda_\pm \frac{\Xi_a}{\tilde{\omega}_a \pm \tilde{\omega}_r - \Xi_a}. \quad (\text{A31})$$

On the transformation, up to the first order in the small parameters λ'_\pm , the Hamiltonian becomes

$$\begin{aligned} \frac{\hat{\mathcal{H}}}{\hbar} \approx & \tilde{\omega}_r a^\dagger a - \frac{\tilde{\Xi}_r}{2} a^{\dagger 2} a^2 + \tilde{\omega}_a b^\dagger b - \frac{\tilde{\Xi}_a}{2} b^{\dagger 2} b^2 \\ & - \tilde{K} a^\dagger a b^\dagger b - \tilde{g}_2 (a^{\dagger 2} b + b^\dagger a^2). \end{aligned} \quad (\text{A32})$$

The approximations here are as in Eq. (A22).

Consider renormalizations in the Hamiltonian (A32). The atom frequency becomes

$$\tilde{\omega}_a = \omega'_a - 2\lambda_+ \lambda'_+ \Xi_a. \quad (\text{A33})$$

The atom anharmonicity renormalizes as

$$\tilde{\Xi}_a = \Xi'_a - 2 \left(\lambda_- \lambda'_- - 4\lambda_+ \lambda'_+ - 6\lambda_+^2 \right) \Xi_a. \quad (\text{A34})$$

Again, we assume that it renormalizes negligibly, i.e. $\tilde{\Xi}_a \approx \Xi_a$.

The cross-Kerr coupling strength dresses as

$$\begin{aligned} \tilde{K} = & K' + 2(\lambda_- \lambda'_- + \lambda_+ \lambda'_+) \Xi_a \\ \approx & K_{0,X} + 2(\lambda'_- g_- + \lambda'_+ g_+) \\ & + 2(\zeta_+ g_+ - \zeta_- g_-) + 2(\lambda_+ - \lambda_-) F \\ & + 4\lambda_r^2 \Xi_a + 4\lambda_2 (g_2 + 2\lambda_2 \Xi_a) \\ & + 4\eta_+ (\tilde{G}_2^+ + 4\eta_+ \Xi_a) + 4\eta_- (\tilde{G}_2^- + 4\eta_- \Xi_a). \end{aligned} \quad (\text{A35})$$

We have used Eqs. (A27) and (A31) in the derivation of Eq. (A36). The second term in Eq. (A35) describes the corrections due to the higher-order nonresonant interactions as in the Hamiltonian Eq. (A29). In Eq. (A36), we retain the corrections of the sixth order in the zero-point fluctuations $\varphi_{r,\text{zpf}}$ and $\varphi_{a,\text{zpf}}$. Although these terms are formally beyond the accuracy of the Hamiltonian Eq. (18), they may be relevant as discussed in Sec. IV D.

Now we plug Eqs. (A21) and (A31) into Eq. (A36). With that, we obtain Eq. (37) in Sec. IV D with the contributions as in Eqs. (38)–(41).

The calculations in this subsection are required to obtain the correct limit for the dispersive shift for the two-level atom as explained in the main text. More precisely, it is the second term in Eq. (A35) which ensures that. However, as we neglect the terms due to nonlinear interactions in $\delta\hat{\mathcal{H}}'_1$ in Eq. (A29), we do not reproduce this limit for the nonlinear-induced cross-Kerr shifts.

c. Resonator anharmonicity negligible in resonance condition

Next, we neglect the resonator anharmonicity in the Hamiltonian (A32) and obtain the renormalized two-photon Hamiltonian (26). We discuss this approximation for two cases:

a. *Wide-line case.* The neglected term provides a shift in the resonance frequency. One case it is negligible is when the artificial atom linewidth is much wider. That may be relevant, for example, when the artificial atom acts as a Josephson photomultiplier [29, 31, 75, 85] and its line is widened due to fast transitions out of the metastable states.

b. *Narrow-line case.* In the other case, characteristic for qubits, the artificial atom linewidth does not overcome the shift from the term we drop in Eq. (A32). In that case we compare this shift to the two-photon coupling rate g_2 .

We expect the resonator anharmonicity to be small, i.e. $n_r |\tilde{\Xi}_r| \ll |\tilde{g}_2|$. For small E_J^c/E_L^r , anharmonicity is expressed as in Eq. (A10). We obtain

$$\frac{\tilde{\Xi}_r}{g_2} \approx \frac{E_C^r}{E_L^r} \frac{\frac{10}{3} \frac{E_J^c}{E_L^r} \sin \delta + 2 \cot \delta}{\varphi_{r,\text{zpf}}^2 \varphi_{a,\text{zpf}}}. \quad (\text{A37})$$

The magnitude of this ratio steadily increases when departing from the closest zero point at $\delta_0 \bmod 2\pi \approx \pm(\pi/2 + \alpha/2)$ with $\alpha = 5E_J^c/3E_L^r$. In the linear approximation,

$$\frac{n_r \tilde{\Xi}_r}{g_2} \approx \frac{E_C^r}{E_L^r} \frac{2n_r}{\varphi_{r,\text{zpf}}^2 \varphi_{a,\text{zpf}}} (\delta_0 - \delta). \quad (\text{A38})$$

We discuss the implications of neglecting the resonator anharmonicity in Sec. VI for the circuit parameters as in the main text.

Appendix B: Calculation of the main cross-Kerr correction with the Wick's theorem

On the transformations in Appendix A, the interactions we are interested in pick up corrections. Each transformation is designed to compensate the direct action of a nonresonant coupling in the resulting frame. With a nonlinear nonresonant coupling, that requires a polynomial of the same order in the transformation exponent. When a transformation is complicated, such as in Eq. (A2), it

becomes nontrivial to trace the origin of the interaction renormalizations.

That is especially concerning when we use our theory for a phase qubit as in Sec. V. Its metastable well holds a finite amount of energy states; hence a virtual process climbing too high does not occur as predicted by our anharmonic oscillator model. It is then of interest to determine how far up the processes in each correction do climb.

In this appendix, we demonstrate how to use the Wick's theorem [86, 87] to calculate the coupling corrections. That provides some grounding for laying out the virtual processes in the diagrams in Figs. 2 and 3. For the phase qubit as in Sec. V, the most vivid correction due to the virtual processes appears in the cross-Kerr coupling strength. We, therefore, focus on the cross-Kerr correction here.

1. Calculation

Beforehand, it is convenient to rewrite Eq. (A2) as

$$\mathcal{S}_a = -\frac{2}{3}(b^\dagger - b)^3 + (b^\dagger + b)^2(b^\dagger - b) - 2(b^\dagger + b). \quad (\text{B1})$$

With this form, the commutators in the BCH formula (A3) are easy to calculate, as our Hamiltonian in Eqs. (14) and (18) depends on the dimensionless canonical coordinates $b^\dagger + b$ and $i(b^\dagger - b)$.

Below we show that dressing of the coupling energy

$$I_{20} = \hbar g_2 (a + a^\dagger)^2 (b + b^\dagger) \quad (\text{B2})$$

quadratic in the resonator operators [see Eq. (18)] gives rise to the cross-Kerr coupling. More precisely, the cross-Kerr correction in Eqs. (35) and (36) arises from expanding the transformation exponent to the first order in Λ_a ,

$$I_{20} \rightarrow e^{-\Lambda_a \mathcal{S}_a} I_{20} e^{\Lambda_a \mathcal{S}_a} \approx I_{20} + \Lambda_a (I_{20} \mathcal{S}_a - \mathcal{S}_a I_{20}). \quad (\text{B3})$$

Here $\Lambda_a = X_a / \omega_a^p$ as defined in Eq. (A1).

While it is trivial to calculate our commutator in Eq. (B3), the calculation can become more involved for higher nonlinearities. We use the Wick's theorem as it makes the manual treatment tractable for more complex cases. Additionally, the Wick's theorem yields the result in normal order.

Thus, we use it to calculate the correction—i.e. of last term in the right-hand side of Eq. (B3). We denote

$$P = b^\dagger + b, \quad M = b^\dagger - b. \quad (\text{B4})$$

Then, noting that only single contractions bring the terms with $b^\dagger b$, we write them out for

$$\begin{aligned} (b^\dagger + b)\mathcal{S} = & -\frac{2 \times 3}{3} : \overline{PMMM} : - \frac{2}{3} C_3^2 : \overline{PMMM} : \\ & + 3 : \overline{PPPM} : - C_3^2 : \overline{PPPM} : + \dots \quad (\text{B5}) \end{aligned}$$

and

$$\mathcal{S}(b^\dagger + b) = 2 : \overline{PPMP} : - : \overline{PPMP} : + \dots, \quad (\text{B6})$$

where $C_n^k = n!/[k!(n-k)!]$ denotes a binomial coefficient, $: O :$ denotes the operation of normal ordering applied to an operator O , and contraction is defined as $\overline{AB} = \overline{AB} - : AB :$.

In Eq. (B5), the first two terms are the contractions with the first term $-2M^3/3$ in Eq. (B1). The other two are the contractions with the second term P^2M there. In Eq. (B6), both terms are due to the second term P^2M in Eq. (B1). Each contraction coefficient includes a factor that counts the contractions alike, such as $: \overline{PMMM} : , : \overline{PMMM} : ,$ and $: \overline{PMMM} :$ for the first term in Eq. (B5).

We note that $\overline{PP} = 1$, $\overline{MM} = -1$, and $\overline{MP} = -1$. Then using Eqs. (B5) and (B6), one can check that the cross-Kerr term proportional to $a^\dagger a b^\dagger b$ comes with a coefficient of $24g_2\Lambda_a$ in Eq. (B3). That is the same coefficient as in Eqs. (35) and (A12) according to the calculation of the correction in Appendix A.

2. Diagrams and the number of energy levels

The atom part of the diagram in Fig. 2(II) shows the process as described, among others, by the term $: \overline{PMMM} :$ similar to the second term in Eq. (B5). Contraction in a term corresponds to a loop in the diagram. Note that, when only taking into account the first BCH commutator as in Eq. (B3), the processes from different interactions do not mix.

The normal-ordered products as in Eqs. (B5) and (B6) directly provide the cross-Kerr coupling Hamiltonian in a convenient form. The Wick's theorem automatically takes into account that the bb^\dagger products in Eq. (B3) yield the normally-ordered $b^\dagger b$. The associated use of commutation relations—bosonic in our case—is exact within the model; however, with it we lose the information on how far up in the energy ladder a process goes.

Based on the structure of the normally-ordered terms in Eqs. (B5) and (B6), we can recover that from Eq. (B3). In the case of the cross-Kerr correction, we simply notice that some of the $b^\dagger b$ processes actually arise from the bb^\dagger ones that bring the atom higher in its energy levels. One such sequence is depicted in Fig. 2(II) with dashed lines.

Note that, for determining the number of energy states required, one can consider normally-ordered I_{20} and \mathcal{S}_a in Eq. (B3). In this form, each of them describe processes that excite the atom as low as possible, while still providing the required results. For example, consider the case when the next higher energy state decays faster than the interaction can occur, due to the reasons *beyond* our simple anharmonic oscillator model. In that case, normally-ordered coupling energy $: I_{20} :$ still correctly describes

the relevant interactions. Same considers \mathcal{S}_a : which is responsible in Eq. (B3) for an approximate unitary transformation.

That is not the case for further normal ordering in the equation. Suppose we have directly substituted \mathcal{S}_a : or I_{20} : into Eq. (B3). In this expression, the order of operators can matter: if the excitations in \mathcal{S}_a : or I_{20} : bring the atom into e.g. a rapidly decaying state, the

respective process yields a different state. Our approximate unitary transformation does not work as intended, as the corresponding (virtual) processes occur differently. However, these very processes are supposed to yield the interactions in the transformed picture. Therefore, if we further normal-order Eq. (B3), that would hide this issue and may predict interaction terms in the Hamiltonian with remarkably incorrect amplitudes or even structure.

-
- [1] E. T. Jaynes and F. W. Cummings, Comparison of quantum and semiclassical radiation theories with application to the beam maser, *Proc. IEEE* **51**, 89 (1963).
- [2] F. Yan, P. Krantz, Y. Sung, M. Kjaergaard, D. L. Campbell, T. P. Orlando, S. Gustavsson, and W. D. Oliver, Tunable coupling scheme for implementing high-fidelity two-qubit gates, *Phys. Rev. Appl.* **10**, 054062 (2018).
- [3] E. A. Sete, A. Q. Chen, R. Manenti, S. Kulshreshtha, and S. Poletto, Floating tunable coupler for scalable quantum computing architectures, *Phys. Rev. Appl.* **15**, 064063 (2021).
- [4] F. Marxer, A. Vepsäläinen, S. W. Jolin, J. Tuorila, A. Landra, C. Ockeloen-Korppi, W. Liu, O. Ahonen, A. Auer, L. Belzane, V. Bergholm, C. F. Chan, K. W. Chan, T. Hiltunen, J. Hotari, E. Hyyppä, J. Ikonen, D. Janzso, M. Koistinen, J. Kotilahti, T. Li, J. Luus, M. Papic, M. Partanen, J. Rähinä, J. Rosti, M. Savvitskiy, M. Seppälä, V. Sevriuk, E. Takala, B. Tarasinski, M. J. Thapa, F. Tosto, N. Vorobeva, L. Yu, K. Y. Tan, J. Hassel, M. Möttönen, and J. Heinsoo, Long-distance transmon coupler with CZ-gate fidelity above 99.8%, *PRX Quantum* **4**, 010314 (2023).
- [5] L. Abdurakhimov, J. Adam, H. Ahmad, O. Ahonen, M. Algaba, G. Alonso, V. Bergholm, R. Beriwal, M. Beuerle, C. Bockstiegel, *et al.*, Technology and performance benchmarks of IQM's 20-qubit quantum computer, arXiv preprint arXiv:2408.12433 (2024).
- [6] J. Koch, T. M. Yu, J. Gambetta, A. A. Houck, D. I. Schuster, J. Majer, A. Blais, M. H. Devoret, S. M. Girvin, and R. J. Schoelkopf, Charge-insensitive qubit design derived from the Cooper pair box, *Phys. Rev. A* **76**, 042319 (2007).
- [7] F. Solgun and S. Srinivasan, Direct calculation of ZZ interaction rates in multimode circuit quantum electrodynamics, *Phys. Rev. Appl.* **18**, 044025 (2022).
- [8] R. W. Boyd, *Nonlinear Optics*, 3rd ed. (Academic Press, 2008).
- [9] S. Haroche, Cavity quantum electrodynamics: a review of Rydberg atom-microwave experiments on entanglement and decoherence (1999) pp. 45–66.
- [10] P. Carbonaro, G. Compagno, and F. Persico, Canonical dressing of atoms by intense radiation fields, *Phys. Lett. A* **73**, 97 (1979).
- [11] A. Blais, R.-S. Huang, A. Wallraff, S. M. Girvin, and R. J. Schoelkopf, Cavity quantum electrodynamics for superconducting electrical circuits: An architecture for quantum computation, *Phys. Rev. A* **69**, 062320 (2004).
- [12] A. Blais, J. Gambetta, A. Wallraff, D. I. Schuster, S. M. Girvin, M. H. Devoret, and R. J. Schoelkopf, Quantum-information processing with circuit quantum electrodynamics, *Phys. Rev. A* **75**, 032329 (2007).
- [13] A. Blais, A. L. Grimsmo, S. M. Girvin, and A. Wallraff, Circuit quantum electrodynamics, *Rev. Mod. Phys.* **93**, 025005 (2021).
- [14] Y. Nakamura, Y. A. Pashkin, and J. S. Tsai, Rabi oscillations in a Josephson-junction charge two-level system, *Phys. Rev. Lett.* **87**, 246601 (2001).
- [15] J. Lisenfeld, *Experiments on superconducting Josephson phase quantum bits*, Ph.D. thesis, Universität Erlangen-Nürnberg (2007).
- [16] S. Ashhab, J. R. Johansson, and F. Nori, Rabi oscillations in a qubit coupled to a quantum two-level system, *New Journal of Physics* **8**, 103 (2006).
- [17] L. Garziano, R. Stassi, V. Macrì, A. F. Kockum, S. Savasta, and F. Nori, Multiphoton quantum Rabi oscillations in ultrastrong cavity QED, *Phys. Rev. A* **92**, 063830 (2015).
- [18] A. Välimaa, W. Crump, M. Kervinen, and M. A. Siljanpää, Multiphonon transitions in a quantum electromechanical system, *Phys. Rev. Appl.* **17**, 064003 (2022).
- [19] M. Ayyash, X. Xu, S. Ashhab, and M. Mariani, Driven multiphoton qubit-resonator interactions, *Phys. Rev. A* **110**, 053711 (2024).
- [20] E. V. Stolyarov, V. L. Andriichuk, and A. M. Sokolov, Two-photon coupling via Josephson element: Breaking the symmetry with magnetic fields, *Phys. Rev. B* **111**, 214517 (2025).
- [21] W. Qin, A. F. Kockum, C. S. Muñoz, A. Miranowicz, and F. Nori, Quantum amplification and simulation of strong and ultrastrong coupling of light and matter, *Physics Reports* **1078**, 1 (2024).
- [22] A. M. Sokolov and F. K. Wilhelm, Superconducting detector that counts microwave photons up to two, *Phys. Rev. Applied* **14**, 064063 (2020).
- [23] A. M. Sokolov, *Photon counting in the microwave domain and its applications to superconducting qubit readout*, Ph.D. thesis, Universität des Saarlandes (2023).
- [24] E. V. Stolyarov and R. A. Baskov, *Detector of microwave photon pairs based on a Josephson photomultiplier* (2025), arXiv:2504.15950 [quant-ph].
- [25] S. Felicetti, J. S. Pedernales, I. L. Egusquiza, G. Romero, L. Lamata, D. Braak, and E. Solano, Spectral collapse via two-phonon interactions in trapped ions, *Phys. Rev. A* **92**, 033817 (2015).
- [26] A. F. Linskens, I. Holleman, N. Dam, and J. Reuss, Two-photon Rabi oscillations, *Phys. Rev. A* **54**, 4854 (1996).
- [27] R. Khan, F. Massel, and T. T. Heikkilä, Cross-Kerr nonlinearity in optomechanical systems, *Phys. Rev. A* **91**, 043822 (2015).
- [28] M. Esposito, A. Ranadive, L. Planat, and N. Roch, Perspective on traveling wave microwave parametric amplifiers, *Applied Physics Letters* **119**, 120501 (2021).

- [29] Y.-F. Chen, D. Hover, S. Sendelbach, L. Maurer, S. T. Merkel, E. J. Pritchett, F. K. Wilhelm, and R. McDermott, Microwave photon counter based on Josephson junctions, *Phys. Rev. Lett.* **107**, 217401 (2011).
- [30] L. C. G. Govia, E. J. Pritchett, S. T. Merkel, D. Pineau, and F. K. Wilhelm, Theory of Josephson photomultipliers: Optimal working conditions and back action, *Phys. Rev. A* **86**, 032311 (2012).
- [31] A. Opremcak, I. V. Pechenezhskiy, C. Howington, B. G. Christensen, M. A. Beck, E. Leonard, J. Suttle, C. Wilen, K. N. Nesterov, G. J. Ribeill, T. Thorbeck, F. Schlenker, M. G. Vavilov, B. L. T. Plourde, and R. McDermott, Measurement of a superconducting qubit with a microwave photon counter, *Science* **361**, 1239 (2018).
- [32] A. Opremcak, C. H. Liu, C. Wilen, K. Okubo, B. G. Christensen, D. Sank, T. C. White, A. Vainsencher, M. Giustina, A. Megrant, B. Burkett, B. L. T. Plourde, and R. McDermott, High-fidelity measurement of a superconducting qubit using an on-chip microwave photon counter, *Phys. Rev. X* **11**, 011027 (2021).
- [33] V. I. Shnyrkov, A. P. Shapovalov, V. Y. Lyakhno, A. O. Dumik, A. A. Kalenyuk, and P. Febvre, An RF SQUID readout for a flux qubit-based microwave single photon counter, *Superconductor Science and Technology* **36**, 035005 (2023).
- [34] O. A. Ilinskaya, A. I. Ryzhov, and S. N. Shevchenko, Flux qubit based detector of microwave photons, *Phys. Rev. B* **110**, 155414 (2024).
- [35] G. Oelsner, C. K. Andersen, M. Reháč, M. Schmelz, S. Anders, M. Grajcar, U. Hübner, K. Mølmer, and E. Il'ichev, Detection of weak microwave fields with an underdamped Josephson junction, *Phys. Rev. Applied* **7**, 014012 (2017).
- [36] A. D'Elia, A. Rettaroli, S. Tocci, D. Babusci, C. Barone, M. Beretta, B. Buonomo, F. Chiarello, N. Chikhi, D. Di Gioacchino, G. Felici, G. Filatrella, M. Fistul, L. Foggetta, C. Gatti, E. Il'ichev, C. Ligi, M. Lisitskiy, G. Maccarrone, F. Mattioli, G. Oelsner, S. Pagano, L. Piersanti, B. Ruggiero, G. Torrioli, and A. Zagoskin, Stepping closer to pulsed single microwave photon detectors for axions search, *IEEE Transactions on Applied Superconductivity* **33**, 1 (2023).
- [37] R. Grimaudo, D. Valenti, B. Spagnolo, G. Filatrella, and C. Guarcello, Josephson-junction-based axion detection through resonant activation, *Phys. Rev. D* **105**, 033007 (2022).
- [38] K. Inomata, Z. Lin, K. Koshino, W. D. Oliver, J.-S. Tsai, T. Yamamoto, and Y. Nakamura, Single microwave-photon detector using an artificial Λ -type three-level system, *Nat. Commun.* **7**, 12303 (2016).
- [39] R. Lescanne, S. Deléglise, E. Albertinale, U. Réglade, T. Capelle, E. Ivanov, T. Jacqmin, Z. Leghtas, and E. Flurin, Irreversible qubit-photon coupling for the detection of itinerant microwave photons, *Phys. Rev. X* **10**, 021038 (2020).
- [40] L. Balembois, J. Travesedo, L. Pallegoix, A. May, E. Billaud, M. Villiers, D. Estève, D. Vion, P. Bertet, and E. Flurin, Cyclically operated microwave single-photon counter with sensitivity of 10^{-22} W/ $\sqrt{\text{Hz}}$, *Phys. Rev. Appl.* **21**, 014043 (2024).
- [41] C. Guerlin, J. Bernu, S. Deléglise, C. Sayrin, S. Gleyzes, S. Kuhr, M. Brune, J.-M. Raimond, and S. Haroche, Progressive field-state collapse and quantum non-demolition photon counting, *Nature* **448**, 889 (2007).
- [42] B. R. Johnson, M. D. Reed, A. A. Houck, D. I. Schuster, L. S. Bishop, E. Ginossar, J. M. Gambetta, L. DiCarlo, L. Frunzio, S. M. Girvin, and R. J. Schoelkopf, Quantum non-demolition detection of single microwave photons in a circuit, *Nat. Phys.* **6**, 663 (2010).
- [43] P. J. Leek, M. Baur, J. M. Fink, R. Bianchetti, L. Steffen, S. Filipp, and A. Wallraff, Cavity quantum electrodynamics with separate photon storage and qubit readout modes, *Phys. Rev. Lett.* **104**, 100504 (2010).
- [44] S. Kono, K. Koshino, Y. Tabuchi, A. Noguchi, and Y. Nakamura, Quantum non-demolition detection of an itinerant microwave photon, *Nature Physics* **14**, 546 (2018).
- [45] A. Essig, Q. Ficheux, T. Peronnin, N. Cottet, R. Lescanne, A. Sarlette, P. Rouchon, Z. Leghtas, and B. Huard, Multiplexed photon number measurement, *Phys. Rev. X* **11**, 031045 (2021).
- [46] R. Dassonneville, R. Assouly, T. Peronnin, P. Rouchon, and B. Huard, Number-resolved photcounter for propagating microwave mode, *Phys. Rev. Applied* **14**, 044022 (2020).
- [47] J. C. Curtis, C. T. Hann, S. S. Elder, C. S. Wang, L. Frunzio, L. Jiang, and R. J. Schoelkopf, Single-shot number-resolved detection of microwave photons with error mitigation, *Phys. Rev. A* **103**, 023705 (2021).
- [48] J. Liu, H.-T. Chen, and D. Segal, Quantum non-demolition photon counting with a hybrid electromechanical probe, *Phys. Rev. A* **102**, 061501 (2020).
- [49] A. Ciani, B. M. Terhal, and D. P. DiVincenzo, Hamiltonian quantum computing with superconducting qubits, *Quantum Sci. Technol.* **4**, 035002 (2019).
- [50] C. Sukumar and B. Buck, Multi-phonon generalisation of the Jaynes-Cummings model, *Physics Letters A* **83**, 211 (1981); S. Singh, Field statistics in some generalized Jaynes-Cummings models, *Phys. Rev. A* **25**, 3206 (1982).
- [51] C. J. Villas-Boas and D. Z. Rossatto, Multiphoton Jaynes-Cummings model: Arbitrary rotations in Fock space and quantum filters, *Phys. Rev. Lett.* **122**, 123604 (2019).
- [52] M. Aspelmeyer, T. J. Kippenberg, and F. Marquardt, Cavity optomechanics, *Rev. Mod. Phys.* **86**, 1391 (2014).
- [53] T. Botter, D. W. C. Brooks, N. Brahms, S. Schreppler, and D. M. Stamper-Kurn, Linear amplifier model for optomechanical systems, *Phys. Rev. A* **85**, 013812 (2012).
- [54] M. F. Dumas, B. Groleau-Paré, A. McDonald, M. H. Muñoz-Arias, C. Lledó, B. D'Anjou, and A. Blais, Measurement-induced transmon ionization, *Phys. Rev. X* **14**, 041023 (2024).
- [55] T. Hillmann and F. Quijandría, Designing Kerr interactions for quantum information processing via counter-rotating terms of asymmetric Josephson-junction loops, *Phys. Rev. Appl.* **17**, 064018 (2022).
- [56] S. Bravyi, D. P. DiVincenzo, and D. Loss, Schrieffer-Wolff transformation for quantum many-body systems, *Annals of Physics* **326**, 2793 (2011).
- [57] D. Zueco, G. M. Reuther, S. Kohler, and P. Hänggi, Qubit-oscillator dynamics in the dispersive regime: Analytical theory beyond the rotating-wave approximation, *Phys. Rev. A* **80**, 033846 (2009).
- [58] F. Beaudoin, J. M. Gambetta, and A. Blais, Dissipation and ultrastrong coupling in circuit QED, *Phys. Rev. A* **84**, 043832 (2011).
- [59] A. M. Sokolov and E. V. Stolyarov, Single-photon limit of dispersive readout of a qubit with a photodetector, *Phys.*

- Rev. A* **101**, 042306 (2020).
- [60] M. Steffen, M. Ansmann, R. McDermott, N. Katz, R. C. Bialczak, E. Lucero, M. Neeley, E. M. Weig, A. N. Cleland, and J. M. Martinis, State tomography of capacitively shunted phase qubits with high fidelity, *Phys. Rev. Lett.* **97**, 050502 (2006).
- [61] E. Jeffrey, D. Sank, J. Y. Mutus, T. C. White, J. Kelly, R. Barends, Y. Chen, Z. Chen, B. Chiaro, A. Dunsworth, A. Megrant, P. J. J. O'Malley, C. Neill, P. Roushan, A. Vainsencher, J. Wenner, A. N. Cleland, and J. M. Martinis, Fast accurate state measurement with superconducting qubits, *Phys. Rev. Lett.* **112**, 190504 (2014).
- [62] R. Zhao, S. Park, T. Zhao, M. Bal, C. McRae, J. Long, and D. Pappas, Merged-element transmon, *Phys. Rev. Appl.* **14**, 064006 (2020).
- [63] L. Neumeier, M. Leib, and M. J. Hartmann, Single-photon transistor in circuit quantum electrodynamics, *Phys. Rev. Lett.* **111**, 063601 (2013).
- [64] R. Shillito, A. Petrescu, J. Cohen, J. Beall, M. Hauru, M. Ganahl, A. G. Lewis, G. Vidal, and A. Blais, Dynamics of transmon ionization, *Phys. Rev. Appl.* **18**, 034031 (2022).
- [65] M. Trif and P. Simon, Photon cross-correlations emitted by a Josephson junction in two microwave cavities, *Phys. Rev. B* **92**, 014503 (2015).
- [66] S.-l. Ma, J.-k. Xie, Y.-l. Ren, X.-k. Li, and F.-l. Li, Photon-pair blockade in a Josephson-photonics circuit with two nondegenerate microwave resonators, *New Journal of Physics* **24**, 053001 (2022).
- [67] M. O. Scully and M. S. Zubairy, *Quantum Optics* (Cambridge University Press, Cambridge, 1997).
- [68] G. P. Berman and A. A. Chumak, Influence of external fields and environment on the dynamics of a phase-qubit-resonator system, *Phys. Rev. A* **83**, 042322 (2011).
- [69] O. O. Chumak and E. V. Stolyarov, Phase-space distribution functions for photon propagation in waveguides coupled to a qubit, *Phys. Rev. A* **88**, 013855 (2013).
- [70] A. Metelmann and A. A. Clerk, Nonreciprocal photon transmission and amplification via reservoir engineering, *Phys. Rev. X* **5**, 021025 (2015).
- [71] Y.-P. Wang and C.-M. Hu, Dissipative couplings in cavity magnonics, *Journal of Applied Physics* **127**, 130901 (2020).
- [72] H.-P. Breuer and F. Petruccione, *The theory of open quantum systems* (Oxford University Press, New York, 2002).
- [73] A. M. Sokolov and T. T. Heikkilä, Signatures and characterization of dominating Kerr nonlinearity between two driven systems with application to a suspended magnetic beam, *Phys. Rev. B* **109**, 014408 (2024).
- [74] S. Stenholm, *Foundations of laser spectroscopy* (John Wiley & Sons, 1984).
- [75] M. Schöndorf, L. C. G. Govia, M. G. Vavilov, R. McDermott, and F. K. Wilhelm, Optimizing microwave photodetection: input-output theory, *Quantum Sci. Technol.* **3**, 024009 (2018).
- [76] J. M. Martinis, S. Nam, J. Aumentado, K. M. Lang, and C. Urbina, Decoherence of a superconducting qubit due to bias noise, *Phys. Rev. B* **67**, 094510 (2003).
- [77] T. P. Orlando, J. E. Mooij, L. Tian, C. H. van der Wal, L. S. Levitov, S. Lloyd, and J. J. Mazo, Superconducting persistent-current qubit, *Phys. Rev. B* **60**, 15398 (1999).
- [78] R. Dassonneville, T. Ramos, V. Milchakov, L. Planat, E. Dumur, F. Foroughi, J. Puertas, S. Leger, K. Bharadwaj, J. Delaforce, C. Naud, W. Hasch-Guichard, J. J. Garcia-Ripoll, N. Roch, and O. Buisson, Fast high-fidelity quantum nondemolition qubit readout via a nonperturbative cross-Kerr coupling, *Phys. Rev. X* **10**, 011045 (2020).
- [79] N. E. Frattini, U. Vool, S. Shankar, A. Narla, K. M. Sliwa, and M. H. Devoret, 3-wave mixing Josephson dipole element, *Applied Physics Letters* **110**, 222603 (2017).
- [80] E. V. Stolyarov, O. V. Kliushnichenko, V. S. Kovtoniuk, and A. A. Semenov, Photon-number resolution with microwave Josephson photomultipliers, *Phys. Rev. A* **108**, 063710 (2023).
- [81] K. Petrovnin, J. Wang, M. Perelshtein, P. Hakonen, and G. S. Paraoanu, Microwave photon detection at parametric criticality, *PRX Quantum* **5**, 020342 (2024).
- [82] G. Zhu, D. G. Ferguson, V. E. Manucharyan, and J. Koch, Circuit QED with fluxonium qubits: Theory of the dispersive regime, *Phys. Rev. B* **87**, 024510 (2013).
- [83] J. Feist and contributors, *QuantumAlgebra.jl* (2021).
- [84] L. D. Landau and E. M. Lifshits, *Quantum Mechanics: Non-Relativistic Theory* (Butterworth-Heinemann, New York, 1991).
- [85] L. C. G. Govia, E. J. Pritchett, C. Xu, B. L. T. Plourde, M. G. Vavilov, F. K. Wilhelm, and R. McDermott, High-fidelity qubit measurement with a microwave-photon counter, *Phys. Rev. A* **90**, 062307 (2014).
- [86] G. C. Wick, The evaluation of the collision matrix, *Phys. Rev.* **80**, 268 (1950).
- [87] P. Blasiak, A. Horzela, K. A. Penson, A. I. Solomon, and G. H. E. Duchamp, Combinatorics and Boson normal ordering: A gentle introduction, *American Journal of Physics* **75**, 639 (2007).